UNIVERSITÀ DEGLI STUDI DI PADOVA

UNIVERSITA' DEGLI STUDI DI PADOVA

Dipartimento di Ingegneria Industriale DII

Corso di Laurea Magistrale in Ingegneria Meccanica

Analysis of the turbulent wake flow of a linear compressor cascade using RANS simulations

Prof. Ernesto Benini
Univ.-Prof. Dr.-Ing. Peter Jeschke
M.Sc Johannes Deutsch

Stefano Regazzo 2027737

Anno Accademico 2022/2023

Abstract

The development of turbomachinery components for aircraft engines and power generation relies heavily on the usage of computational fluid dynamics (CFD). Due to the high number of simulations required in design optimizations, the Reynolds-averaged Navier-Stokes (RANS) approach with turbulence modelling will be the industry standard for many years to come as it offers fast turnaround times. However, the semi-empirical turbulence models were developed and calibrated for rather simple canonical flows with simplifying assumptions, whereas the flow in turbomachines, particularly in off-design operation, is complex and at a time difficult to predict. On the other hand, scale resolving methods like Large Eddy Simulation (LES) and Direct Numerical Simulation (DNS) are presently limited in an industrial context, as they require a high computational effort to (partially) resolve all turbulent spatial and temporal scales. However, in research context, LES and DNS simulations are feasible for selected configurations and operating points. The LES and DNS results of these cases can assess the validity of lower order turbulence models and contribute to the model development. Within the scope of this thesis, the mixing process of a turbulent wake flow of a compressor blade is investigated with the RANS $k-\omega$ turbulence model and compared to the results of an LES simulation of the same geometry. This works aims to identify deficits of the turbulence model formulations in the wake region and to highlight approaches to improve the investigated turbulence models. Starting with a literature review, the flow features of a turbulent wake flow are identified and described. Next, the RANS study is performed on a compressor cascade. First, a turbulence inflow study is conducted to provide similar operating condition with respect to the LES. Afterwards, in order to separate the errors predicted in the wake flow and the errors introduced in the cascade passage by the RANS simulations, the LES is post-processed to derive suitable inlet boundary conditions downstream of the trailing edge for the RANS simulation wake domain. A grid study is performed to ensure grid independent results. The total pressure loss coefficient, the strain rate tensor, the Reynolds stress tensor and its anisotropy are the inspected flow quantities in the comparison between the RANS and LES simulations. The results show that the $k-\omega$ model is able of capturing the total pressure loss and the strain rate tensor, while the turbulence state shows deviations with the LES and it is not capable to accurately reproduce the Reynolds stress tensor and its anisotropy.

Contents

List of Figures

List of Tables

Symbols

Simbol	Description	Unit
α	Flow angle	grad
β_s	Stagger angle	grad
c_p	Specific heat at constant pressure	J/Kg K
c_v	Specific heat at constant volume	J/Kg K
D_k	Destruction term of turbulent kinetic energy	[-]
e	Specific internal energy	m/s^2
h	Specific enthalpy	m/s^2
k	Turbulent kinetic energy	m/s^2
l	Length	m
Tu	Turbulence intensity	[-]
L_t	Turbulent length scale	m
M	Mach number	[-]
P_k	Production term of turbulent kinetic energy	J/kg
p	Static pressure	Pa
P_t	Total pressure	Pa
Pr	Prandtl number	[-]
T	Temperature	K
q_{ij}	Heat-flux vector	J/m^2 s
Re	Reynolds number	[-]
S	Sutherland constant	K
s	entropy	J/kg
$\widetilde{u_i'' u_j''}$	Reynolds stress tensor components	J/kg
t	time	s
u, v, w	Velocity components	m/s
y^+	Wall-distance	[-]
x, y, z	Cartesian coordinates	m
$1, 2, 3\zeta$	Streamwise Cartesian coordinates	m
x_i	position vector in index notation	m
δ	Boundary layer thickness	m
δ^*	Displacement thickness	m
δij	Kronecker Delta	[-]
γ	numerical intermittency	[-]
ϵ	Turbulent dissipation rate	m/s^2
η	Kolmogorov lengthscale	m^2
k	Wavenumber	[-]
λ_c	Thermal conductivity	m
λ	Stoke's hypothesis	Pa s
λ_k	Wavelength	m
μ	Dynamic viscosity	Pa s
μ_T	Eddy viscosity	Pa s
ν	Kinematic viscosity	m^2s
$\widetilde{E_{ij}}$	Shear-rate tensor for RANS	1/s
$\overline{S_{ij}}$	Shear-rate tensor for LES	1/s

$\widetilde{\Omega_{ij}}$	Rotational tensor for RANS	1/s
$\overline{\Omega_{ij}}$	Rotational tensor for LES	1/s
$\sigma_i j$	Viscous stress tensor	m/s^2
τ	Timescale	s
τ_{ij}	Reynolds stress tensor	m/s^2
τ_{wall}	Wall shear stress	Pa
Θ	Momentum thickness	m
ω	Specific turbulent dissipation rate	1/s
ω_{loss}	Reynolds stress tensor	m/s^2
$\underline{\phi}$	Variable for LES	[-]
$\overline{\phi}$	Filtered part for LES	[-]
ϕ'	Residual quantity for LES	[-]
$\widetilde{\phi}$	Favre average for LES	[-]
ϕ''	Fluctuation part (Favre average) for LES	[-]
Φ	Variable for RANS	[-]
$\overline{\Phi}$	Reynolds average	[-]
Φ'	Fluctuation part (Reynolds average)	[-]
$\widetilde{\Phi}$	Favre average for RANS	[-]
Φ''	Fluctuation part (Favre average) for RANS	[-]

Indices

0	Reference value
1	Inflow state
2	Outflow state
T	Total
loss	Total pressure loss
∞	Free stream value

Abbreviations

CFD	Computational Fluid Dynamics
DNS	Direct Numerical Simulation
GTF	Geared Turbofan
LES	Large-Eddy-Simulation
HPC	High-Pressure-Compressor
LPT	Low-Pressure-Turbine
Cut1.5	Measurement Plane at 150% of the chord length
Cut2	Measurement Plane at 200% of the chord length
NS	Navier-Stokes-Equations
RANS	Reynolds-(Favre)Averaged-Navier-Stokes-Equations
RST	Reynolds-Stress-Tensor
SGS	Subgrid-Scale-Model
STG	Synthetic turbulence generator
TKE	Turbulent Kinetic Energy
VB	Viscous blending
WALE	Wall-Adapting Local Eddy- viscosity
N	Number of Cells
L.E.	Leading edge
T.E.	Trailing edge
S.S.	Suction side
P.S.	Pressure side

1 Riassunto Esteso

Lo sviluppo di componenti di turbomacchine per motori aeronautici e per la generazione di energia si basa principalmente sull'uso della fluidodinamica computazionale. A causa dell'elevato numero di simulazioni necessarie per la loro ottimizzazione, l'approccio Reynolds-averaged Navier-Stokes (RANS) con modelli di turbolenza verrà utilizzato nel settore industriale per molti anni a venire. Tuttavia, i modelli di turbolenza semi-empirici sono stati sviluppati e calibrati per flussi relativamente semplici con varie ipotesi semplificative, mentre il flusso nelle turbomacchine, in particolare nel funzionamento fuori progetto, è complesso e talvolta difficile da prevedere. D'altra parte, i metodi scale resolving, come la Large Eddy Simulation (LES) o la Direct Numerical Simulation (DNS), sono attualmente limitati a bassi numeri di Reynolds nel contesto industriale, poiché richiedono un elevato sforzo computazionale per risolvere (parzialmente) tutte le scale spaziali e temporali della turbolenza. Tuttavia, nell'ambito della ricerca, le simulazioni LES e DNS sono attuabili per configurazioni e punti operativi selezionati. Diverse ricerche hanno provato l'affidabilità delle simulazioni LES e DNS, che possono essere utilizzate per assicurare la validità dei modelli di turbolenza di ordine inferiore e contribuire al loro sviluppo.

In questa tesi viene studiato il processo di miscelazione della scia turbolenta di una schiera di pale di un compressore utilizzando il modello di turbolenza RANS $k-\omega$, per poi confrontare i risultati con quelli di una simulazione LES della stessa geometria. Questo lavoro mira a identificare i deficit dei modelli di turbolenza e a fornire approcci per migliorarli. Si parte da un'analisi teorica in merito alle caratteristiche del flusso di una scia turbolenta. In seguito, viene ricavato il setup numerico per le simulazioni RANS. In primo luogo, per confrontare e valutare i risultati RANS, viene condotto uno studio sul decadimento del livello di turbulenza in ingresso, garantendo così condizioni operative simili rispetto alla LES. Da questa analisi vengono ricavati i valori più idonei dell'intensità di turbulenza e della scala degli "eddy". Successivamente, per separare gli errori introdotti nella zona di scia e quelli nel passaggio del fluido all'interno del canale palare nelle simulazioni RANS, la simulazione LES viene post-processata per ricavare le condizioni al contorno d'ingresso per il dominio di scia della simulazione RANS, collocato a valle del bordo di uscita della schiera di pale. Poiché varie ricerche affermano che la variabile ω nel modello di turbulenza $k-\omega$ non ha nessun significato fisico e ha valori completamente diversi da quelli della simulazione LES, l'approccio "Frozen" è utilizzato: si tratta di una procedura che permette di preservare i valori delle variabili della simulazione LES (pressione totale, velocità, pressione, etc...), ma di risolvere l'equazione di trasporto per ω nell'intero dominio della schiera, utilizzando le variabili di turbulenza precedentemente scelte. Conseguentemente, viene eseguita l'operazione di estrazione dei dati in modo tale da fornire le varibili in ingresso al dominio della sola scia. Per garantire risultati indipendenti dal livello di densità della Mesh adottata, viene svolta un'analisi di sensitivtà della griglia "Mesh Sensitivity Analysis", utilizzando il coefficiente di perdita di pressione totale come variabile dello studio, seguendo la procedura "Grid Convergence Method" (ASME).

Il coefficiente di perdita di pressione totale, il tensore di deformazione, il tensore degli

sforzi di Reynolds e la sua anisotropia sono le quantità fluidodinamiche prese in considerazione nel confronto tra le simulazioni RANS e LES. L'indagine rivela che la RANS riesce a predire le perdite di pressione totale rispetto alla LES, mostrando solo una piccola discrepanza nella zona centrale della scia e sulla larghezza di quest'ultima, ma non in una misura tale da compromettere il processo di progettazione e ottimizzazione. Inoltre, il tensore di deformazione è stato analizzato all'interno di un sistema di coordinate cartesiane allineato con la direzione del flusso, mostrando che la RANS è in grado di catturare ogni componente, nonostante una piccola variazione nella pendenza in corrispondenza del lato in depressione man mano che la scia si sviluppa più a valle. Riguardo al tensore degli sforzi di Reynolds, la simulazione RANS non riesce a predire l'andamento delle componenti rispetto alla LES. Per ottenere una miglior panoramica degli sforzi di Reynolds, la sua anisotropia è visualizzata utilizzando l'assegnazione dei colori di Emory e Iaccarino (2014) applicata alla mappa baricentrica di Banerjee et al. (2007). Lo stato turbulento può essere isotropo 3C (tre componenti), anisotropo 2C (due componenti), anisotropo 1C (una componente), o una combinazione di questi tre stati. La simulazione RANS mostra un significativo stato di turbolenza 2C, soprattutto nella regione di scia vicino alla regione di flusso indisturbato, che tende a conservarsi verso l'uscita, mentre la LES rileva uno stato turbolento 2C del deflusso, che passa ad uno più isotropo 3C.

In conclusione, il modello $k-\omega$ è in grado di prevedere la perdita di pressione totale e il tensore di deformazione, quindi il tensore degli sforzi viscosi medio. Al contrario, lo stato turbolento mostra discrepanze con la LES e non è in grado di riprodurre accuratamente il tensore degli sforzi di Reynolds e la sua anisotropia. Pertanto, le piccole deviazioni nel rimescolamento della scia e nella distribuzione della perdita di pressione totale sono probabilmente legate alle differenze negli sforzi di Reynolds.

Questa ricerca apre alla possibilità di studiare la scia utilizzando i modelli di trasporto degli sforzi di Reynolds o i modelli algebrici espliciti degli sforzi di Reynolds (EARSM) e di confrontare i risultati con il modello standard $k-\omega$. Inoltre, il presente studio fornisce una possibile guida per le future estensioni dei modelli basati sulla "eddy viscosity", in quanto evidenzia le principali carenze del modello nel riprodurre una corretta topologia della turbolenza nella regione della scia.

2 Introduction

Within this chapter, the motivation of this thesis is introduced first. Afterwards, the state of the art regarding current engine developments and the aerodynamic of High-pressure-compressor cascade (HPC) is presented, as well as numerical methods employed for simulating compressors. Objectives and the outlines of the thesis are given at the end of this chapter.

2.1 Motivation

The development of turbomachinery components for aircraft engines plays a major role in aircraft propulsion systems both in turbofan and turboprop engines. For the aviation industry, the Advisory Council for Aviation Research and Innovation in Europe (ACARE) has developed diverse aims in reducing greenhouse emissions and ensuring a sustainable mobility [23]. Compressors and turbines have a significant influence on the fuel consumption, as the latter depends on the aerodynamic efficiency of the engine and its weight. With a focus on the compressor, the trend in design optimization is to push towards highly-loaded compressor blades, in order to reduce the number of stages. By doing so, the boundary layers on the blades of compressors and fans are exposed to an higher adverse pressure gradient, that can lead to the detachment of the fluid flow and compromise the engine performance, in particular during off-design operation. To take account of that, the blade design leads to a reduction in the aspect ratio (blade length to chord) and an increase in the solidity (chord to pitch ratio) of the blades resulting in shorter deeper blades. Nevertheless, a reduce in efficiency is presented at the design point due to the increased boundary layer length, though there is an improvement in the pressure rise. Consequently, in order to design both lighter and more efficient engines, as well as quieter, it is essential to understand the fluid dynamic processes within these machines.

As experimental researches are challenging to perform on turbomachinery components, as they provide limited access to the flow for measurement equipment and requires long setups, the Computational Fluid Dynamics (CFD) [15] represents the most commonly used tool in industrial and research areas for solving fluid problems, since it offers expeditious detailed view on characteristic flow phenomenons and gives strong insights into the main fluid flow properties. By means of this, the usage of CFD for numerically solving the governing equations of fluid dynamics opens a great potential in investigate and optimizing a great numbers of different geometries, thus achieving the exposed aims.

Within the industrial sector, Reynolds-Averaged-Navier-Stokes (RANS) methods remain the standard approach for design and optimization process, as the solution generated with RANS-Methods represents a low-cost solution method [55]. However, the accuracy of RANS-based CFD predictions heavily depends on the ability of the closure models to

take account of the effect of all unsteadiness, stochastic and deterministic, on the mean flow field. Thus, the development of such predictions is a main challenge and an active research area, where Large Eddy Simulation (LES) and Direct Numerical Simulation (DNS) are widely used as "Numerical experiments" [40].

By means of this, the presented work focuses in the wake region by comparing RANS results with an LES simulation and to underline the main discrepancies in regards of the main wake characteristics.

2.2 State of the Art

Thanks to geared Turbofan (GTF), the trend of modern subsonic engine concepts is in developing Turbofan with ultra-high bypass (UHB) engines, with bypass ratio in 12–15 range [13]. Nowadays, conventional turbofan engines offer a bypass ratio of 8-10. The main idea behind is an increased propulsion efficiency due to the additional integrated fan powered by the low-pressure turbine (LPT), meaning that part of the incoming air bypasses the core engine. The advantages of employing the Turbofan are engine length size and weight reduction, increased efficiency, improved off-design operation and reduced noise emissions. Moreover, axial compressors and fans provide mechanical compression for the air stream that enters the aircraft engine and they are extremely sensitive to the operating condition, which can results in critical conditions such as stall or chocking of the entire engine. Therefore, the research focused on understanding the phenomenon that governs the loss mechanism and the exchange of energy with the fluid flow, and providing the tools to achieve a better design and optimization process. An overview of the work done in the past years is given in the following section.

2.2.1 Airflow Analysis over Compressor Cascades

Within subsonic compressor cascade, various source of losses arise, such as passage vortex, leading edge horseshoe vortex and blade trailing edge vortex [20] as shown in figure 2.1. There are three main zones of interest in regards of the compressor blade: the mid section, the hub flow and the tip flow. In the mid-section of the blade passage, the flow is assumed to be two-dimensional. By moving towards both the hub or casing, the end wall boundary layers of the blade passage generate mean spanwise flows, leading to complex three-dimensional flows. Near the hub or blade attachment point, the interaction of the hub boundary layer and blade boundary layer causes root vortex interactions, while at the tip of the blade, various three-dimensional flow structures arise due to tip gap flows and casing boundary layer interactions. In addition to the fundamental flow structures of a single blade, incoming wakes from upstream blade rows interact with the blade boundary layer and end wall region.

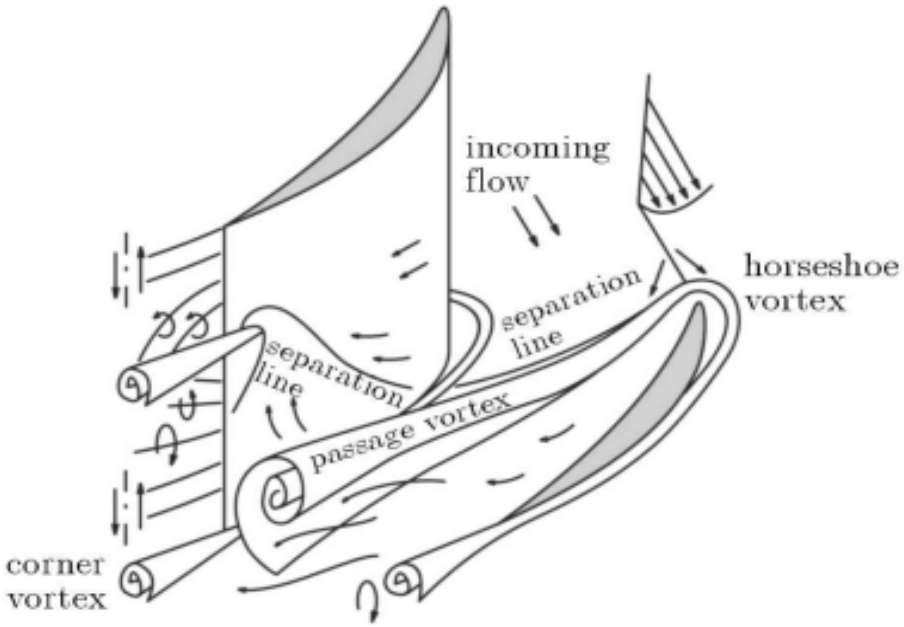

Figure 2.1: Schematic overview of secondary flow structure topology (Kang and Hirsch, 1991 [20])

Since this thesis focuses on the mixing out of the wake, an overview of the work done on zone is presented in the following .

Considerable researches have been conducted to understand flow phenomena in the wake region. Lieblein et al. [30] provided a simple equation expressing the wake momentum thickness of conventional low-speed cascade blades, derived from boundary-layer theory in conjunction with simplifying approximations, that was used to gain an insight into qualitative effects on stalling. Lowson [31] presented a general theoretical analysis of compressor noise for the discrete-frequencies sound radiated by axial-flow fans and compressors. It is to mention that the predominant radiation mechanism is via the fluctuating forces on the blade, that are directly connected to the wakes passing effect. The study aims to give a tool in the preliminary design stage of an engine to minimize the the noise by choosing an appropriate number of rotors and stators blades, as well as rotational speed. Raj and Lakshminarayana [41] studied the near and far wake characteristics of a cascade of airfoils by analyzing the mean velocity, turbulence intensity and Reynolds stress across the wake at several distances downstream of the cascade, revealing that the wake is asymmetrical. Moreover, The wake edge velocity changes continuously, giving rise to either slower decay of the wake defect or faster decay. Reynolds et al. [42] conducted an experimental investigation on the wake of a fan rotor blade. Results show that radial, tangential and axial velocity defects in the rotor wake decay very rapidly in the trailing-edge region and large radial velocities in the near-wake region, indicating a large radial migration of momentum and energy. Furthermore, increased blade loading slows the decay rates of tangential and axial velocity defects. Adamczyk [1] presented a research in which the unsteady flow process associated with the recovery of the total pressure deficit of a wake as it passes through a blade row was delineated. The impact of the recovery

process on wake mixing can play an important role on the efficiency of a stage. The wakes that pass through a blade row before being mixed-out by viscous diffusion can reduce the wake mixing loss by as much as seventy percent. In more recent studies, according to Halstead et al. [59], the effects of wake passing suppress the laminar separation bubble because of the existence of a calmed region. The resulting effect is the reduction of profile losses. Shi et al. [48] conducted a research on the unsteady behavior of the wake when blade suction side separation is located close to the trailing edge in a compressor cascade. Results reveal that under the influence of laminar separation vortex shedding [21], the suction side of the wake shows slower velocity recovery in comparison with the pressure side of the wake and that the dominant flow loss is produced by the wake instability and the laminar vortex shedding.

2.2.2 Numerical Methods

With the advent of modern computers and large clusters, the CFD is able to perform simulations on engine Reynolds number flows of relevant geometries. However, within the industrial field, the accuracy of the CFD methodology employed is still limited. The Reynolds-Averaged-Navier-Stokes (RANS) methods are still widely used as it provides a trade-off between computational time and valid results. Moreover, the RANS models have been tuned to provide better accuracy for specific flows. Nevertheless, RANS modelling only provides statistically averaged results and does not simulate instantaneous flow features, meaning that it can lead to misleading "loss bucket" [13] and inaccurate design optimization. The prediction of unsteady phenomenon, such as wake interaction, have also been studied with unsteady RANS. According to Lardeau and Leschziner [25], the mesh resolution requirements need to be substantially increased to capture the unsteady features of interest, leading to lower computational efficiency. Furthermore, a tendency for unsteady RANS to overestimate the coherence of unsteady structures, resulting in poor turbulent energy prediction of the wakes.

Instead, scale-resolving-simulations (SRS) come into account, like Large Eddy Simulation (LES) and Direct Numerical Simulation (DNS), to predict unsteadiness, large and small turbulent structures and vortexes. Currently the use of DNS is still too computationally expensive for compressor design condition, especially within the industrial context. In the research field, the DNS is feasible and it leads to to unmatched accuracy [40], as all the scales of motion are resolved. Regarding the Large-Eddy-Simulations (LES), only the large scales of motion are resolved, whereas the smallest turbulent structures are modeled [54]. It represents a cost benefit compared to DNS, but LES still requires a high amount of computational resources and thus remains in the field of research applications [39]. Although the LES models the small scales of turbulence, studies has proven the reliability of this method. You et al. [58] conducted a study on the impact of tip clearance on cascade losses by utilizing Large Eddy Simulation (LES). The obtained results showed improvements in predicting the decay and Reynolds stresses of the vortex over previous studies employing RANS methods, as well accurately traced the trajectory and evolution of the tip clearance vortex.

More recent research works, Medic et al. [33] investigated the performance of LES in capturing flow properties such as transition when compared with experimental data for a range of different airfoil shapes. The study showed LES performed well in predicting the transition and boundary layer behaviour and for the evaluation of loss of different profile designs. Moreover, Legget [27] focused on a single compressor cascade stage and on the effects variation in inflow incidence and free-stream flow conditions have on the stages' performance. The results showed to what processes loss is attributed and how this loss varies over the incidence range, and secondly highlighted the differences in loss attribution of the breakdown between RANS and LES.

In this thesis, the RANS results are compared with an LES, as the LES simulations is proving to be useful in investigating unsteady effects that were previously overlooked in RANS studies.

It is worth mentioning that within this thesis the "Frozen Approach" is used that was first introduced by Parneix [38] in backward-facing step case-study. This "a priori" test is one in which a model is assessed outside of its full predictive context. The objective of a priori testing is to remove ambiguities or inaccuracies that occur in solutions of the full set of equations, such as numerical errors and inaccuracies in terms additional to those being tested. The study consisted of isolating the turbulence model by solving the full transport equation for one isolated component of the Reynolds stress tensor and preserve the mean flow field that can be taken from a DNS data base. The results showed that the main problem comes from the Reynolds stress transport equation, which gives an over-prediction of the turbulent force, and not from both Daly-Harlow transport model for k [9], and the ϵ-equation, as they do perform well, to the contrary of what is generally thought in the literature.

2.3 Objectives and Outline of the thesis

As high fidelity simulations are still too expensive for commercial design, industry relies on RANS. This present study aims to identify the deficiencies in predicting the turbulence topology in the wake region of one of the most used turbulence model, the $k-\omega$ by Wilcox, and to highlight approaches to improve it by comparing the results with an LES simulation of the same geometry. By means of this, the RANS simulation that is used for the comparison, is performed by using inlet flow variables that arise from the LES data set downstream of the trailing edge as boundary condition. The resulting operation ensures the separation between the error generated by the wake flow and the error introduced by RANS in respect of the transitional flow around the blade (fig. 2.2). The inspected flow field quantities are the total pressure loss coefficient, the strain rate tensor, the Reynolds stress tensor and its anisotropy.

Chapter 3 presents the theoretical background in detail and it introduces the fundamental governing equations of fluid dynamics. Moreover, an insight about the logic and numerical methods employed to resolve the equations of RANS and LES are given, as well as a brief

theoretical framework of the turbulent wake flow. In chapter 4, the RANS study is conducted on the NACA 65 V103-220 compressor cascade. Hence, a turbulence inflow study is conducted in order to provide similar operating condition with respect to the LES. Afterwards, the "Frozen Approach" is used to derive suitable boundary condition for the wake domain simulation and thus isolate the wake flow behaviour, followed by a grid independence study. In chapter 5 the comparison between the RANS and LES simulations is presented. Finally, the thesis outcome is summarized and an outlook is provided in chapter 6.

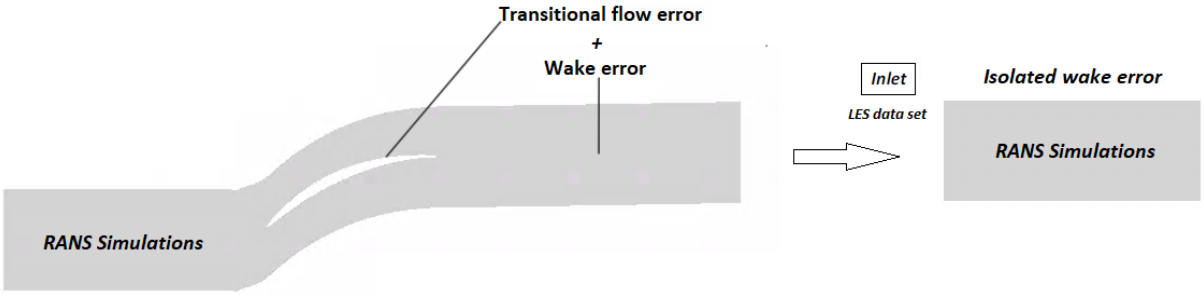

Figure 2.2: Schematic representation of the procedure to isolate the wake flow error (not to scale).

3 Fundamentals of Compressible Fluids

The present chapter provides a theoretical background regarding turbulence flow and its related properties. The primary objective of this thesis is to distinguish and delineate the main differences between Reynolds-(Favre)Averaged-Navier-Stokes (RANS) and Large Eddy Simulation (LES) approach in the wake region. To do so, an insight into the numerical methods employed to solve the Navier-Stokes equations is presented, and an overview of the fundamental theory of turbulent wake flow is considered.

3.1 Navier-Stokes Equations

The governing equations of fluid flow represent mathematical statements of the conservation laws of physics:

- Conservation of mass: the rate of change of mass in a fluid element equals the net rate of flow into the fluid element
- Newton's second law: the rate of change of momentum equals the sum of the forces on a fluid particle
- First law of thermodynamics: the rate of change of energy of a fluid particle is equal to the rate of heat addition to the fluid particle plus the rate of work done on the particle

The fluid is regarded as a continuum, calorically ideal and perfect gas. The behaviour of the fluid is described in terms of macroscopic properties, such as velocity, pressure, density and temperature, and their space and time derivatives. Moreover, the operating fluid is considered as a "Newtonian fluid", meaning that the viscous stresses are proportional to the rates of deformation. The gravitational forces are neglected. With these assumptions, it is possible to obtain the unsteady conservative form of Navier-Stokes-Equations as follows:

$$\frac{\partial \rho}{\partial t} + \frac{\partial \rho u_i}{\partial x_i} = 0 \tag{3.1}$$

$$\frac{\partial \rho u_i}{\partial t} + \frac{\partial \rho u_i u_j}{\partial x_j} = -\frac{\partial p}{\partial x_i} + \frac{\partial \sigma_{ij}}{\partial x_{ij}} \tag{3.2}$$

$$\frac{\partial}{\partial t}\left[\rho\left(e + \frac{u_i\, u_i}{2}\right)\right] + \frac{\partial}{\partial x_j}\left[\rho u_j\left(h + \frac{u_i\, u_i}{2}\right)\right] = \frac{\partial}{\partial x_j}\left[u_i\, \sigma_{ij} - q_j\right] \tag{3.3}$$

with the u_i represents the velocity, x_i the spatial coordinate, ρ the density, t the time, p the pressure, q_j the heat-flux and σ_{ij} is the viscous stress tensor. The variable e governs the specific internal energy, which takes part in the definition of the specific enthalpy, defined as:

$$h = e + \frac{p}{\rho} \tag{3.4}$$

Considering Einstein's summation convention [11] regarding the Kronecker symbol δ_{ij} (δ_{ij} = 1 for i = j and δ_{ij} = 0 otherwise), the viscous stress tensor can be expressed as:

$$\sigma_{ij} = 2\mu E_{ij} - \lambda \left(\frac{\partial u_k}{\partial x_k} \right) \delta_{ij}. \tag{3.5}$$

In this equation, λ is defined according to the Stoke's hypothesis as:

$$\lambda = -\frac{2}{3}\mu, \tag{3.6}$$

where μ is the dynamic viscosity and the term E_{ij}, which is the strain-rate tensor, is defined as:

$$E_{ij} = \frac{\left(\frac{\partial u_i}{\partial x_j} + \frac{\partial u_j}{\partial x_i} \right)}{2}. \tag{3.7}$$

Regarding the heat-flux, it is determined with the following equation:

$$q_j = -\lambda_c \frac{\partial T}{\partial x_j} \tag{3.8}$$

whereas, λ_c is the thermal conductivity of the fluid and T is the temperature.

As previously mentioned, the operating fluid within this research is air, assumed as ideal gas. The state of an ideal gas is considered in thermodynamic equilibrium by means of just two state variables, so it is possible to determine it with the Equation of State:

$$p = \rho R T \tag{3.9}$$

in which R is the specific ideal gas constant.

Under this assumptions, the specific internal energy e can be described by the following equation:

$$e = c_v T \tag{3.10}$$

whereas c_v is the the specific heat at constant volume, while the dynamic viscosity is defined by the Sutherland's law:

$$\mu = \mu_0 \frac{T_0 + S}{T + S} \left(\frac{T}{T_0} \right)^{\frac{3}{2}}, \tag{3.11}$$

with consideration of the reference viscosity $\mu_0 = 1.7198 \cdot 10^{-5}$ the Sutherland's constant $S = 110K$ and the reference temperature $T_0 = 273K$.

In the flow of compressible fluids, the equations of state provide the linkage between the energy equation on one hand and mass conservation and momentum equations on the other. This linkage arises through the possibility of density variations as a result of pressure and temperature variations in the flow field.

Navier-Stokes equations describe all states of the flow, which can be laminar or turbulent. In order to determinate the regime state of a fluid flow, Reynolds Number [43] is used. The Reynolds number of a flow gives a measure of the relative importance of inertia forces (associated with convective effects) and viscous forces:

$$Re = \frac{\rho u L}{\mu} \tag{3.12}$$

whereas, ρ represents the density, u represents the velocity, L the characteristic length dimension and μ the dynamic viscosity. Depending upon the value of that number, it is possible to state if the regime is laminar or turbulent [35]:

- Laminar regime: the flow is smooth and adjacent layers of fluid slide past each other in an orderly manner. In this scenario, inertial forces are negligible compared with the viscous forces (small Re)

- Turbulent regime: the flow is completely filled with 3D non stationary eddies and fluctuations interval, thus inertial forces are predominant upon the viscous one (high Re)

The investigation is focused on the wake region, which is characterized by a turbulent mixing process. Therefore, an overview regarding the turbulent flow is given in the following chapters.

3.1.1 General Properties of Turbulence

In order to acknowledge the concept of "Turbulence", it is mandatory to provide a definition. Quoting Bradshaw (1971) [8]: “Turbulence is a three dimensional time dependent motion in which vortex stretching causes velocity fluctuations to spread to all wavelengths between a minimum determined by viscous forces and a maximum determined by the boundary conditions."

To better understand this definition, it is possible to split the instantaneous fluid field $\Phi(x_i, t)$ in a constant $\bar{\Phi}(x_i)$ and a time dependent part $\Phi'(x, t)$:

$$\Phi(x_i, t) = \bar{\Phi}(x_i) + \Phi'(x, t) \tag{3.13}$$

The mean part shows a behaviour that is predictable, while, on the other hand, the time dependent part is always three-dimensional and unsteady, thus mandating the use of statistical methods to analyze it.

Most of the time, in the engineering field, the flow properties are integrated in time to extract mean values. However, time-averaging will lead to the closure problem that is analyzed in the section 3.2.1.

As previously said, turbulence consists of a continuous spectrum of scales ranging from largest to smallest or "eddies". A turbulent eddy can be thought of as a local swirling motion. Analyzing a turbulent flow, it is possible to observe that eddies overlap in space, whereas large ones interact with smaller ones. This mechanism leads to what is called a "energy cascade process", which is analysed thoroughly in the following section.

3.1.2 The Kolmogorov Energy Cascade

One of the defining characteristics of turbulent flows is the broad range of scales present in the turbulent structures. The notion of an "energy cascade" was first proposed by Richardson (1922) [45], whereby larger turbulence eddies transfer the Turbulent Kinetic Energy (TKE) to smaller scales through an inviscid process. However, only at the smallest ones, dissipation occurs due to molecular viscosity.

By analyzing a turbulent flow from a macroscopic perspective, its characteristic depends on the geometry that generated it. Instead, at microscopic scales, the behavior of the turbulent flux is homogeneous and isotropic (Universal Equilibrium). Moreover, as the Reynolds number increases, the range of scales in the turbulent structures expands, leading to the break down of larger structures into smaller ones as a result of vortex interactions.

From these considerations, the energy cascade process was investigated in depth and extended by Kolmogorov, resulting in what is now known as Kolmogorov’s Theory (K41)

[22].

To better understand this theory, the dissipative scale η and dissipation rate ϵ are defined. The dissipative scale represents the scale at which Turbulent Kinetic Energy (TKE) is converted into heat, while the dissipation rate represents the rate at which TKE is dissipated by the smallest scales.

Furthermore, the turbulent length scale l, a characteristic velocity $u(l)$, and timescale $\tau(l)$ are defined. According to Kolmogorov's Theory, the velocity $u(l)$ and timescale $\tau(l)$ decrease as a result of the transfer of TKE to smaller scales and the break down of larger structures into smaller length scales l. Therefore, the Reynolds number

$$Re = \frac{u(l)l}{\nu} \tag{3.14}$$

for a given structure, decreases as well, which causes an increase in viscous effects, leading to the dissipation process.

Since turbulence contains a continuous spectrum of scales, it is convenient to think in terms of spectral distribution of energy a shown in the figure 3.1. In general, a spectral representation is a Fourier decomposition [50] into wavenumbers k, or, equivalently, wavelengths:

$$\lambda_w = \frac{2\pi}{k} \tag{3.15}$$

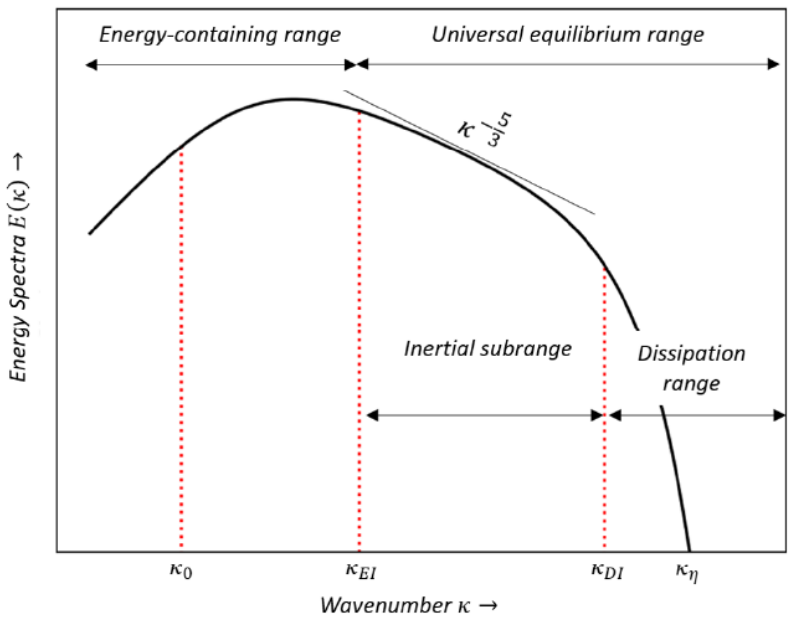

Figure 3.1: Schematic illustration of the energy cascade with the energy spectra over the wavenumber

The first Kolmogorov's hypothesis is as follows: at sufficiently high Reynolds number ($Re >> 1$) and for the small-scale turbulent motions ($l << l_0$), the flux is statistically homogeneous and isotropic.

On the left side of the spectrum, the wavenumber k_0 is associated to the largest scales l_0 and $u(l_0)$, whereas the large eddies are anisotropic and are affected by the boundary conditions of the flow. The characteristic length scale l_{EI} ($l_{EI} \approx \frac{1}{6} l_0$) splits large energy-containing eddies ($l > l_{EI}$) and the small isotropic length scales ($l < l_{EI}$).

In the energy cascade for $l < l_{EI}$ or $k < k_{EI}$, the two dominant processes are the transfer of TKE to smaller scales and viscous dissipation. Thus, the important parameters are the rate at which the small scales receive energy from the large scales $\mathcal{T}_{EI}$ and the kinematic viscosity μ. It is reasonable to assume that the dissipation rate ϵ is nearly the same as the transfer rate of energy $\mathcal{T}_{EI}$. This leads to the **Kolmogorov's first similarity hypothesis**: in every turbulent flow at sufficiently high Reynolds number ($Re >> 1$), the statistics of the small-scale motions ($l < l_{EI}$) have a universal form that is uniquely determined by ϵ and ν. From a pure dimensional analysis, the dissipative Kolmogorov scales in length, velocity and timescale are denoted as follows:

$$\eta = \left(\frac{\nu^3}{\epsilon}\right)^{\frac{1}{4}} \tag{3.16}$$

$$u_\eta = (\nu\epsilon)^{\frac{1}{4}} \tag{3.17}$$

$$\tau_\eta = \left(\frac{\nu}{\epsilon}\right)^{\frac{1}{2}} \tag{3.18}$$

The Reynolds number based on the Kolmogorov scale is unity, expressed as:

$$Re_\eta = \frac{u_\eta \eta}{\nu} = 1. \tag{3.19}$$

This is in agreement with the notion that the energy cascade continues towards smaller and smaller scales until the Reynolds number is low enough for dissipation to occur efficiently. The dissipation rate at this scale is given by:

$$\epsilon_\eta = \nu \left(\frac{u_\eta}{\eta}\right)^2 = \epsilon \tag{3.20}$$

indicating that the energy that reaches the Kolmogorov scale dissipates at the same rate it arrives.

Additionally, as the Reynolds number increases, the spread between the largest and smallest scales becomes larger. The equations that highlight this relationship are:

$$\frac{l_o}{\eta} \sim Re^{3/4} \tag{3.21}$$

$$\frac{u_o}{u_\eta} \sim Re^{1/4} \tag{3.22}$$

$$\frac{\tau}{\tau_\eta} \sim Re^{1/2} \tag{3.23}$$

Finally, **Kolmogorov's second similarity hypothesis** states that in every turbulent flow at sufficiently high Reynolds number ($Re >> 1$), the statistics of the motions of scale l in the range ($l_0 >> l >> \eta$) have a universal form that is uniquely determined by ϵ and independent by ν.

The basis for this hypothesis lies in the observation that eddies in this range are considerable larger than dissipative eddies, leading to significant higher Reynolds numbers in which the viscous effects are neglected.

Thanks to the Kolmgorov's Theory, it is possible to develop models to describe the turbulence behaviour through numerical simulations.

3.2 Numerical Methods

The aim of this chapter is to briefly introduce the logic and numerical methods employed to resolve the equations of RANS, LES and turbulence models. All numerical simulations are conducted using TRACE [4], a solver developed by the German Aerospace Center.

3.2.1 Reynolds-(Favre)Averaged-Navier-Stokes (RANS)

The Reynolds-(Favre)Averaged Navier-Stokes (RANS) approach incorporating turbulence modeling continues to be the prevalent technique numerous industrial applications, due to the low computational effort needed to solve the governing equations. Reynolds decomposition [43] is used in order to split the fluid flow quantities into their mean and fluctuating components, as represented by the equation:

$$\Phi = \bar{\Phi} + \Phi'. \tag{3.24}$$

The averaging operation can be in time, space or whole averaged. The mean part is obtained with the following equation:

$$\bar{\Phi} = \lim_{N\to\infty} \sum_{n=1}^{N} \Phi \tag{3.25}$$

In this present study, a computational investigation is performed on a case of compressible fluid flow. The application of Favre-Averaging [14], a density-weighted averaging technique, is employed into the analysis. This is mathematically expressed as:

$$\widetilde{\Phi} = \frac{1}{\overline{\rho}}\overline{\rho\Phi} \tag{3.26}$$

wherein, the flow quantities at any given instant are split into a Favre-averaged mean and a fluctuating component through the following expression:

$$\Phi = \widetilde{\Phi} + \Phi'' \tag{3.27}$$

Except for the density and pressure, which are split into a mean (time, space or ensemble average) and a fluctuating part, all the other quantities are formulated with the Favre-Averaging:

$$\rho = \overline{\rho} + \rho' \tag{3.28}$$
$$p = \overline{p} + p' \tag{3.29}$$
$$u_i = \widetilde{u}_i + u_i'' \tag{3.30}$$
$$e = \widetilde{e} + e'' \tag{3.31}$$
$$h = \widetilde{h} + h'' \tag{3.32}$$

Applying the averaging method to the N-S equations, the Reynolds-(Favre)Averaged Navier-Stokes (RANS) are obtained:

$$\frac{\partial \overline{\rho}}{\partial t} + \frac{\partial}{\partial x_i}\left(\overline{\rho}\widetilde{u}_i\right) = 0 \tag{3.33}$$

$$\frac{\partial}{\partial t}\left(\overline{\rho}\widetilde{u}_i\right) + \frac{\partial}{\partial x_j}\left(\overline{\rho}\widetilde{u}_j\widetilde{u}_i\right) = -\frac{\partial \overline{p}}{\partial x_i} + \frac{\partial}{\partial x_j}\left[\overline{\sigma_{ij}} - \overline{\rho u_i'' u_j''}\right] \tag{3.34}$$

$$\begin{aligned}\frac{\partial}{\partial t}\left[\overline{\rho}\left(\widetilde{e} + \frac{\widetilde{u}_i\widetilde{u}_i}{2} + \widetilde{\frac{u_i''u_i''}{2}}\right)\right] + \frac{\partial}{\partial x_j}\left[\widetilde{u}_j\overline{\rho}\left(\widetilde{h} + \frac{\widetilde{u}_i\widetilde{u}_i}{2} + \widetilde{\frac{u_i''u_i''}{2}}\right)\right] = \\ \frac{\partial}{\partial x_j}\left[-\overline{q_j} - \overline{\rho}\widetilde{u_j''h''} + \widetilde{\sigma_{ij}u_i''} - \frac{1}{2}\overline{\rho}\widetilde{u_j''u_i''u_i''}\right] + \\ \frac{\partial}{\partial x_j}\left[\widetilde{u}_i\left(\overline{\sigma_{ij}} - \overline{\rho u_i'' u_j''}\right)\right]\end{aligned} \tag{3.35}$$

$$P = \overline{\rho} R \widetilde{T} \tag{3.36}$$

With regards to the derived set of equations, new unknown correlations of fluctuating quantities are emerge. This is the so-called closure problem, where the equations for higher correlations continuously lead to new unknown variables due to the non-linear nature of the problem. In order to solve the equations, Wilcox [55] defined certain correlations, such as the description of the turbulent transport of heat:

$$\overline{q_j} = \overline{\rho u_j'' h''} = -\frac{\mu c_p}{Pr_T} \frac{\partial T}{\partial x_j} \tag{3.37}$$

in which Pr_T is the constant turbulent Prandtl number, while the terms

$$\widetilde{\sigma_{ij} u_i''} - \frac{1}{2} \overline{\rho} \widetilde{u_j'' u_i'' u_i''} \tag{3.38}$$

correspond to molecular diffusion and turbulent transport of turbulence kinetic energy.

Favre-averaged Reynolds-stress symmetric tensor

$$\tau_{ij} = \overline{\rho u_i'' u_j''} \tag{3.39}$$

is defined as the mean transport of momentum due to turbulence. The present term consist of six unknown components.

The most common approach to the closure problem is to relate the Favre-averaged Reynolds-stresses to the mean shear using the Boussinesq approximation:

$$\tau_{ij} = 2\mu_T \left(\widetilde{E_{ij}} - \frac{1}{3} \frac{\partial \widetilde{u_k}}{\partial x_k} \delta_{ij} \right) - \frac{2}{3} \overline{\rho} k \delta_{ij}. \tag{3.40}$$

Hereby, k is defined as the turbulent kinetic energy

$$k = \frac{\widetilde{u_i'' u_i''}}{2}, \tag{3.41}$$

A new unknown variable appears in the Boussinesq approximation called eddy viscosity μ_T. Several turbulence models are available to calculate it. However, the Boussinesq approximation is often not properly valid in complex flows where the mean shear rates are not linearly related to the Reynolds stresses. Despite this, eddy viscosity based models do perform well enough to be useful and form the basis for most commercial RANS solvers.

Since the two-equation model $k-\omega$ by Wilcox (1988) is employed within this work, an insight about this model is given.

In the $k-\omega$ turbulence model for compressible flow, the eddy viscosity is determined in dependency of the turbulent kinetic energy k and the specific dissipation rate ω:

$$\mu_T = \frac{\overline{\rho} k}{\omega} \tag{3.42}$$

By means of this, the specific dissipation rate ω is defined as the ratio of turbulent dissipation rate ϵ and TKE k:

$$\omega = \frac{\epsilon}{k} \tag{3.43}$$

To determine the unknowns, two transport equations of the turbulent kinetic energy k and the specific dissipation rate ω are introduced and have to be solved:

$$\frac{\partial}{\partial t}\left(\overline{\rho} k\right) + \frac{\partial}{\partial x_j}\left(\overline{\rho}\widetilde{u_j} k\right) = P_k - \beta_k \overline{\rho}\omega k + \frac{\partial}{\partial x_j}\left[\left(\mu + \sigma_k \mu_T\right)\frac{\partial k}{\partial x_j}\right] \tag{3.44}$$

$$\frac{\partial}{\partial t}\left(\overline{\rho}\omega\right) + \frac{\partial}{\partial x_j}\left(\overline{\rho}\widetilde{u_j}\omega\right) = \alpha\frac{\omega}{k}\tau_{ij}\frac{\partial \widetilde{u_i}}{\partial x_j} - \beta_\omega \overline{\rho}\omega^2 + \frac{\partial}{\partial x_j}\left[\left(\mu + \sigma_\omega \mu_T\right)\frac{\partial \omega}{\partial x_j}\right] \tag{3.45}$$

Herewith, P_k is defined as the production term

$$P_k = \tau_{ij}\frac{\partial \widetilde{u_i}}{\partial x_j}, \tag{3.46}$$

and D_k is called destruction term and it is determined as follows:

$$D_k = \beta_k \overline{\rho}\omega k. \tag{3.47}$$

The production term P_k represents the rate at which kinetic energy is transferred from the mean flow to the turbulence, while the dissipation one D_k is the rate at which turbulent kinetic energy is converted into thermal internal energy.

The respective closure coefficients are listed below:

$$\alpha = \frac{5}{9}, \quad \beta_k = \frac{9}{100}, \quad \beta_\omega = \frac{3}{40}, \quad \sigma_k = \sigma_\omega = \frac{1}{2} \tag{3.48}$$

To improve the accuracy and the reliability of the $k-\omega$ model, various model extensions exist.

Within this test case, high turbulent intensity levels are present, causing the non-physical behavior of turbulent kinetic energy overproduction. The Kato-Launder modification [26] aims to reduce the tendency to over-predict the turbulent production in regions with large normal strain, for instance on the stagnation points. To do so, the production term P_k is reformulated as shown:

$$\tau_{ij}\frac{\partial \widetilde{u_i}}{\partial x_j} = \mu_T \left|\widetilde{E_{ij}}\right|^2 \approx \mu_T \left|\widetilde{E_{ij}}\right| \left|\widetilde{\Omega}\right| \tag{3.49}$$

with the rotation tensor $\widetilde{\Omega}$

$$\widetilde{\Omega} = \left(\frac{\partial \widetilde{u_i}}{\partial x_j} - \frac{\partial \widetilde{u_j}}{\partial x_i}\right) \tag{3.50}$$

Another model extention used to enhance the capability of the $k-\omega$ turubulent model is the the transition model by Langtry and Menter [24]. It is an empirical method based on two new transport equations $\gamma - Re_\Theta$, in addition to the k and ω equations. Its purpose is to improve the prediction of the transition from laminar to turbulent state in the boundary layers.

The numerical intermittency γ indicates the state of the flow in the boundary layer and it can assume values from zero to one. The transport equation for the intermittency γ is described as follows:

$$\frac{D\overline{\rho}\gamma}{Dt} = \frac{\partial}{\partial x_j}\left[(\mu + \sigma_\gamma \mu_T)\frac{\partial \gamma}{\partial x_j}\right] + P_\gamma - E_\gamma \tag{3.51}$$

The production term P_γ and the destruction source E_γ are defined as follows:

$$P_\gamma = F_{\text{length}} c_{a1} \overline{\rho} S (\gamma F_{\text{onset}})^{0.5} (1 - c_{e1}\gamma) \tag{3.52}$$

$$E_\gamma = c_{a2} \overline{\rho} \Omega \gamma F_{\text{turb}} (1 - c_{e2}\gamma) \tag{3.53}$$

in which F_{length} indicates the transition length, whereas F_{onset} describes the begin of the transition.

Regarding the second equation, the criteria for transition is set based on the local Reynolds number $Re_{\Theta t}$, indicating the transition begin based on the momentum thickness Θ.

$$\frac{D\bar{\rho}\tilde{Re}_{\theta t}}{Dt} = \frac{\partial}{\partial x_j}\left[\sigma_{\theta t}\left(\mu + \mu_T\right)\frac{\tilde{Re}_{\theta t}}{x_j}\right] + P_{\Theta t} \tag{3.54}$$

where the production term $P_{\Theta t}$ is denoted by the following equation:

$$P_{\Theta t} = c_{\theta t}\frac{(\bar{\rho}u)^2}{c_t\mu}(Re_{\theta t} - \tilde{Re}_{\theta t})(1 - F_{\theta t}) \tag{3.55}$$

To account the separation induced transition, the following equation for the separation intermittency γ_{sep} is based on the critical Reynolds number

$$\gamma_{\text{sep}} = \min\left[s_1 \max\left(\frac{Re_v}{3.235Re_{\theta c}} - 1\right)F_{\text{reattach}}, 2\right]F_\theta \tag{3.56}$$

The remaining closure coefficients are described by empirical correlations in .

To complete the setup of the $\gamma - Re_{\Theta t}$ transition model, the effective intermittency

$$\gamma_{\text{eff}} = max(\gamma, \gamma_{\text{sep}}) \tag{3.57}$$

is considered, hence the production and destruction term of the TKE transport equation (3.46) in terms of the $k - \omega$ turbulence model are determined as follows:

$$\tilde{P}_k = \gamma_{\text{eff}}\tilde{P}_k \tag{3.58}$$

$$\tilde{D}_k = min[max(\gamma, 0.1)1.0]\tilde{D}_k. \tag{3.59}$$

The implementation in TRACE is described in [16].

For the $k - \omega$ model, the Viscous Blending Limiter [6] is available. This extension limits the eddy viscosity and thus the production of turbulent kinetic energy in turbulent flows. The eddy viscosity formulation is changed to:

$$\mu_T = \frac{a_1\rho k}{max(a_1\omega,\ b_v S)} \tag{3.60}$$

with $a_1 = 0.31$ and b_v being a detection factor for areas of viscous flow that depends on the model version. S denotes the traceless strain tensor norm of the flow. In the present study, both Viscous blending version 1, in which b_v is defined as

$$b_v = min\left(max\left(\frac{\omega_{Quot}}{500},\ 0.1\right),\ 1\right) \tag{3.61}$$

$$\omega_{Quot} = \omega/\omega_{corr} \tag{3.62}$$

$$\omega_{corr} = k^{-0.613} \tag{3.63}$$

and version 2, where b_v is defined as follows:

$$b_v = min\left(max\left(\frac{2\ atan(\frac{\omega}{\omega_{corr}} + c_2)}{\pi} - c_3\ f_{VRPM,w}, 0\right), 1\right) \tag{3.64}$$

$$\omega_{corr} = \omega_{ref}\left(\frac{k}{k_{ref}}\right)^{-0.613} c_1 \tag{3.65}$$

$$f_{VRPM,w} = min\left(max\left(f_{VRPM}\frac{\Omega_{SW}^2}{\Omega^2}, 0\right), 1\right), \tag{3.66}$$

are employed. Hereby, $c_1 = 1$, $c_2 = 0$,

are model constants, the quantities k_{ref} and ω_{ref} are reference values that are defined as the area average of the respective turbulence model quantities at the inlet panel [17].

3.2.2 Large Eddy Simulations (LES)

Large Eddy Simulation (LES) approach is based on the observation that the larger eddies need to be computed for each problem with a time-dependent simulation, while, for the small-scale turbulent motions, the flux is statistically homogeneous and isotropic [15]. Instead of time-averaging, LES applies a spatial filtering operation to separate the large energy-containing eddies and smaller ones.

First, a spatial filtering operation, by means of a filter function $G_\Delta(r, x)$, is defined with the aim of resolving in an unsteady flow computation all those eddies with a length scale greater than the cutoff width. Eddies below the threshold are modeled. According to Pope [40], it is necessary to resolve at least 80% of the total energy to achieve an acceptable LES solution.

The filtering operation can be described as

$$\overline{\phi} = \int_{R^3} G_\Delta(r,x)\phi(x-r,t)dr$$

where the integration is performed over the entire domain, and the specified filter satisfies the following property:

$$\int_{R^3} G(r,x)dr = 1$$

Applying this filtering to the flow variables results in a set of filtered flow quantities that can be decomposed in a similar manner as the time averaged quantities

$$\phi = \overline{\phi} + \phi' \tag{3.67}$$

in which $\overline{\phi}$ is the filtered variable and ϕ' is the residual quantities.

The application of Favre-filtered quantities is employed into the analysis for the derivation of the LES equations for compressible fluid flow. In this case the Favre filtering is defined in the same manner but now with a spatially filtered density

$$\widetilde{\phi} = \frac{1}{\overline{\rho}}\overline{\rho\phi} \tag{3.68}$$

wherein, the flow quantities at any given instant are split into a Favre-filtered quantity and a residual component through the following expression:

$$\phi = \widetilde{\phi} + \phi'' \tag{3.69}$$

In TRACE, the filter width Δ is set as

$$\Delta = V^{\frac{1}{3}} \tag{3.70}$$

whereby V is the cell volume of the grid.

The filtering operation applied on the conservation laws leads to the so-called filtered Navier-Stokes-equation as follows:

$$\frac{\partial\overline{\rho}}{\partial t} + \frac{\partial}{\partial x_i}\left(\overline{\rho}\widetilde{u}_i\right) = 0 \tag{3.71}$$

$$\frac{\partial}{\partial t}\left(\overline{\rho}\widetilde{u}_i\right) + \frac{\partial}{\partial x_j}\left(\overline{\rho}\widetilde{u}_j\widetilde{u}_i\right) = -\frac{\partial \overline{p}}{\partial x_i} + \frac{\partial}{\partial x_j}\left[\overline{\tau_{ij}} + \overline{\tau_{ij}}^s\right] \tag{3.72}$$

$$\frac{\partial}{\partial t}\left[\overline{\rho}\left(\widetilde{e} + \frac{\widetilde{u}_i\widetilde{u}_i}{2}\right)\right] + \frac{\partial}{\partial x_j}\left[\widetilde{u}_j\overline{\rho}\left(\widetilde{e} + \frac{\widetilde{u}_i\widetilde{u}_i}{2}\right)\right] = \frac{\partial}{\partial x_j}\left[-\overline{q_j} + \overline{u_j\tau_{ij}} - \overline{u_i p}\right] \tag{3.73}$$

Hereby, the filtered viscous stress tensor $\overline{\tau_{ij}}$ is defined as:

$$\overline{\tau_{ij}} = \frac{\mu(\widetilde{T})}{Re_\infty}\left(\overline{S}_{ij} - \frac{2}{3}\overline{S}_{ij}\delta_{ij})\right) \tag{3.74}$$

with the $\overline{S}_{ij}$ represents the filtered strain rate tensor and Re_∞ represents the free stream Reynolds number.

Regarding the filtered heat flux vector, it depends on the Reynolds number Re, the heat capacity ratio γ_r, the Prandtl number Pr, the Mach number M and the filtered temperature $\widetilde{T}$:

$$\overline{q}_j = -\frac{\mu(\widetilde{T})}{(\gamma - 1)\, RePrM^2}\frac{\partial \widetilde{T}}{\partial x_j}. \tag{3.75}$$

Considering the unresolved sub grid scale stress tensor $\overline{\tau_{ij}}^s$, it is given by:

$$\overline{\tau_{ij}}^s = -(\overline{\rho u_i u_j} - \overline{\rho}\widetilde{u}_i\widetilde{u}_j) \tag{3.76}$$

Analogous to the Reynolds-(Favre)averaged Navier-Stokes, in order to solve the closure problem, a sub grid scale model (SGS) needs to be formulated. In this present study, the large eddy simulation has been performed by using the Wall-Adapting Local Eddy-viscosity (WALE) model [36]. Therefore, an overview is given in the following section.

The adopted solver TRACE implements the WALE model according to Nicoud and Ducros, which is based on the square of the velocity gradient tensor $\overline{g}_{ij}$, represented by:

$$\overline{g}_{ij} = \frac{\partial \widetilde{u_i}}{\partial x_j}. \tag{3.77}$$

The description of the SGS stress tensor $\overline{\tau_{ij}}^s$ is made by using the Boussinesq approximation:

$$\tau_{ij} = 2\mu_T\left(\overline{S_{ij}} - \frac{1}{3}\frac{\partial \widetilde{u_k}}{\partial u_k}\delta_{ij}\right) - \frac{2}{3}\overline{\rho}k\delta_{ij}. \tag{3.78}$$

The eddy viscosity μ_T is determined from resolved quantities:

$$\mu_T = \overline{\rho}(C_w\Delta)^2 \frac{(S_{ij}^d S_{ij}^d)^{\frac{3}{2}}}{(S_{ij}S_{ij})^{\frac{5}{2}} + (S_{ij}^d S_{ij}^d)^{\frac{5}{4}}} \tag{3.79}$$

in which the constant C_w is

$$C_w = 0.5587, \tag{3.80}$$

computed from the relation

$$C_w^2 = \alpha C_s^2 \tag{3.81}$$

with $C_s = 0.17$ and the factor α is the average of Table I in [ref...].

The WALE tensor S_{ij}^d is given by

$$S_{ij}^d = \overline{S}_{ik}\overline{S}_{kj} + \overline{\Omega}_{ik}\overline{\Omega}_{kj} - \frac{1}{3}\delta_{ij}(\overline{S}_{nm}\overline{S}_{nm} - \overline{\Omega}_{nm}\overline{\Omega}_{nm}). \tag{3.82}$$

whereby $\overline{\Omega}_{ij}$ the filtered rotation tensor

$$\overline{\Omega}_{ij} = \left(\frac{\partial\widetilde{u_i}}{\partial x_j} - \frac{\partial\widetilde{u_j}}{\partial x_i}\right) \tag{3.83}$$

and $\overline{S}_{ij}$ is the filtered strain rate

$$\overline{S}_{ij} = \left(\frac{\partial\widetilde{u_i}}{\partial x_j} + \frac{\partial\widetilde{u_j}}{\partial x_i}\right) \tag{3.84}$$

The resulting formulation ensure that all the turbulence structures relevant for the kinetic energy dissipation are detected. Moreover, the eddy-viscosity tends to go naturally to zero in the vicinity of a wall, removing the need for any dynamic constant adjustment or damping functions in the computation of wall-bounded flows. Finally, the model is invariant to any coordinate translation or rotation, meaning that it can be used for complex geometries.

3.2.3 Flow solver

The above presented Favre-averaged Navier-Stokes equations and the filtered Navier-Stokes equation are numerically solved by the turbomachinery's flow solver TRACE. Hereby, the cell-centered finite volume method for spatial and temporal discretization is utilized for all simulations [29]. Structured mesh are distributed to different blocks to allow for parallel computation. The finite volume method is based on the integral conservation of the governing equations by applying the Gauss's theorem, leading to the following finite volume discretization scheme [37]:

$$\int_V \frac{\partial \mathbf{q}}{\partial t}\, dV + \oint_{\partial V} (\mathbf{F} \cdot \mathbf{n})\, dA = + \oint_{\partial V} (\mathbf{F}_v \cdot \mathbf{n})\, dA + \int_V \mathbf{S}\, dV \tag{3.85}$$

with the control volume $\mathbf{V}$, the vector of conservative variables $\mathbf{q}$, the inviscid $\mathbf{F}$ and viscid $\mathbf{F}_v$ flux vectors as well as the volume source term $\mathbf{S}$. The balance in equation needs to be fulfilled for each cell in the respective domain. In terms of spatial discretization, in order to solve the the so-called Riemann-Problem (RP) regarding the inviscid fluxes [37], the MUSCL-Scheme (Monotonic Upstream Scheme for Conservation Laws) [19] is implemented.

The numerical setup for both LES and RANS simuations are presented in the relative sections 4.2 and 4.3.

3.3 Fundamental theory of a turbulent wake flow

The aim of this present chapter is to examine the development of turbulent boundary layer in wall-bounded flow for high Reynolds number and the resulting wake. Moreover, an insight regarding Reynolds stress anisotropy and its visualisation is presented.

3.3.1 Turbulent wake flow generation

The process of the boundary layer development can be explained by regarding an airflow over a semi-infinite flat plate model illustrated in the following figure:

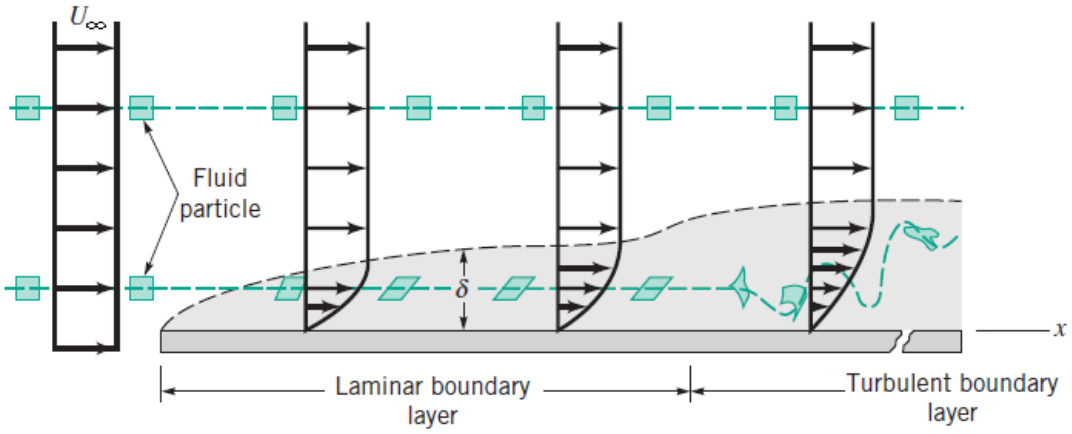

Figure 3.2: Schematic representation of the boundary layer development process on a an exemplary semi-infinite flat plate, by Munson [35]

Hereby, the y coordinate represents the distance from the wall, the x coordinate the flow direction and U_∞ represents the free stream velocity. According to Schlichting et al. [47], the airflow with high Re can be decomposed as an inviscid outer flow area far from the wall and a thin boundary layer close to the wall, in which viscous forces are significant. As already stated, the Reynolds number is representative of the state regime of the flow and for a semi-infinite flat plate is defined as:

$$Re_x = \frac{\rho U_\infty x}{\mu}. \tag{3.86}$$

By observing the airflow, it develops a thin boundary layer of laminar state due to the no-slip condition from the leading edge ($Re_x \approx 1$). With increasing distance from the leading edge, the boundary layer thickness $\delta(x)$ becomes larger, concurrently with the Reynolds number. At some distance downstream from the leading edge, the transition from laminar to turbulent boundary layer flow occurs at a critical value of the Reynolds number, Re_{xcrit}, that can ranging from $2{\cdot}10^5$ to $3{\cdot}10^6$ (Schlichting et al.[47]). Furthermore, according to Schlichting et al., the transition location depends on: the roughness of the surface, the amount of turbulence in the upstream flow, the Reynolds number and the outer flow pressure distribution. After the transition, the boundary layer flow becomes fully turbulent with the emergence of three-dimensional and unsteady eddies.

In the description of the boundary layer along a semi-infinite flat plate, the pressure is constant throughout the fluid. In a compressor cascade, the pressure varies because of the imposed curvature: the decrease in pressure in the direction of flow is termed as *favorable pressure gradient*

$$\left(\frac{\partial u}{\partial x}\right) > 0, \tag{3.87}$$

while the increase in pressure in the direction of flow is termed as *adverse pressure gradient*

$$\left(\frac{\partial u}{\partial x}\right) < 0. \tag{3.88}$$

In presence of *adverse pressure gradient*, a phenomenon commonly referred to *boundary layer separation* can occur: the wall shear stress τ_{wall}, defined as

$$\tau_{wall} = \mu \left(\frac{\partial u}{\partial y}\right)_{y=0}, \tag{3.89}$$

reaches the zero value, leading to the detachment of the fluid from the wall, with a reverse flow in the boundary layer as shown in the following figure:

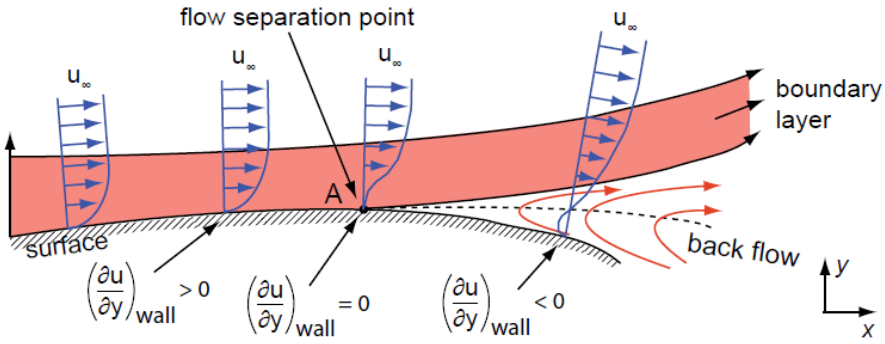

Figure 3.3: Development of the separation zone [52].

The coalescence of boundary layers on the suction and pressure sides at the trailing edge of the blade, along with the separation zone, leads to generation of the turbulent wake flow. Therefore, it is characterized by a velocity and total pressure deficiencies, that are maximum at the center wake and they tend to decrease to zero towards the inviscid outer flow area. The width of the wake increases with increasing distance from the blade because of the diffusion term σ_{ij} in the Navier-Stokes equations, resulting in a turbulent mixing process, that tends to uniform the properties of the fluid flow.

According to Raj and Lakshminarayana [41], another feature of the turbulent wake in a cascade is that it exhibits asymmetry as consequence of loading on the blade. This asymmetry is maintained up to $\frac{3}{4}$ of the chord length from the trailing edge but it depends upon the operating conditions, such as the incidence angle.

3.3.2 Reynolds stress anisotropy

As the following comparison is regarded in terms of the Reynolds stress anisotropy tensor and its invariant, the definiton and its physical meaning is presented. It serves as a measure to describe turbulence anisotropy and it is defined as

$$a_{ij} = \frac{\widetilde{u_i'' u_j''}}{k} - \frac{2}{3}\delta_{ij}. \tag{3.90}$$

Thus, this quantity describes the non-dimensional deviation of the Reynolds stress tensor from the isotropic state

$$\widetilde{u_i'' u_j''} = \frac{2}{3} k \delta ij. \tag{3.91}$$

However, it depends on the chosen coordinate system. Lumley (1979) used the invariants of a_{ij} and its constraints to visualize the state of turbulence, which are independent of the coordinate system. In this research, the barycentric map of Banerjee et al. (2007) is used in conjuction with the Emory and Iaccarino (2014) color map assignmenet [12]. Therefore, an insight of this turbulence anisotropy visulization technique is given.

The turbulence state can be described by a linear combination of the three limiting turbulence states: one-component (1C), isotropic two-component (2C) and isotropic (3C). In the Isotropic 3C turbulence, the anisotropy is forced to be zero. The Isotropic 2C turbulence represents a turbulence state in which only two fluctuating components of equal intensity exist. Finally, the one-component turbulence (1C) is characterized by one fluctuating component which dominates over the other two.

In principal coordinates, the spectral theorem states that the anisotropy tensor can be constructed as a linear combination

$$a_{ij} = C_{1C} a_{1C} + C_{2C} a_{2C} + C_{3C} a_{3C} \tag{3.92}$$

with

$$C_{1C} = \lambda_1 - \lambda_2 \qquad C_{2C} = 2(\lambda_2 - \lambda_3) \qquad C_{3C} = 3\lambda_3 + 1, \tag{3.93}$$

whereby, the eigenvalues $\lambda_1 > \lambda_2 > \lambda_3$ are used to compute the weights C_{iC} of the linear combination of the three limiting turbulent states 1C, 2C and 3C.

To visualize the Reynolds stress anisotropy, the weights C_{iC} of turbulent states are mapped to the RGB channels, where, red is assigned to 1C, green is assigned to isotropic 2C and

blue is assigned to isotropic 3C. The RGB barycentric map is shown in the following figure:

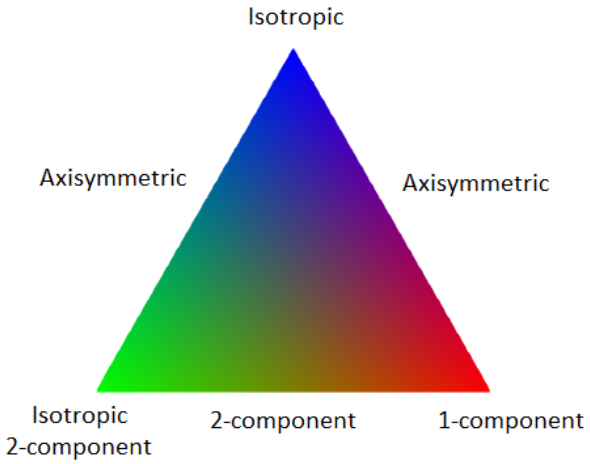

Figure 3.4: Reynolds stress anisotropy contours plotted in the anisotropy invariant barycentric map

4 RANS-Study of NACA65 cascade

The following chapter summarizes the performed RANS simulations study. First, the geometry of the cascade is outlined. Afterwards, the numerical setup of the NACA65 cascade is provided for both RANS and LES approaches. The methodology to achieve a correct turbulent inflow boundary conditions for the RANS simulations is presented, according to the available LES data. Second, the frozen approach is performed to extract the input data for the wake domain. Finally, a grid study is conducted in the wake region to ensure a grid independent results.

4.1 Overview of NACA65 cascade

For both RANS and LES, simulations are performed on a NACA 65 V103-220 compressor cascade, which is representative of the mid-span section of a rotor blade in a highly loaded axial compressor. Leipold et al. [28] and Hilgenfeld and Pfitzner [18] conducted researches on regards of this airfoil performance by specifically examining the midspan section of a linear cascade rig. The researchers chose this approach to reduce the impact of complex flow interactions resulting from end walls and tip leakages. The experiments cover design and off-design incidence as well as the impact of incoming wakes.

In this present study, the LES simulation performed by Deutsch [10] is used as high fidelity data to highlight the deficiencies of RANS simulations. The geometry and the operating conditions employed in this analysis are outlined in Tab. 4.1.

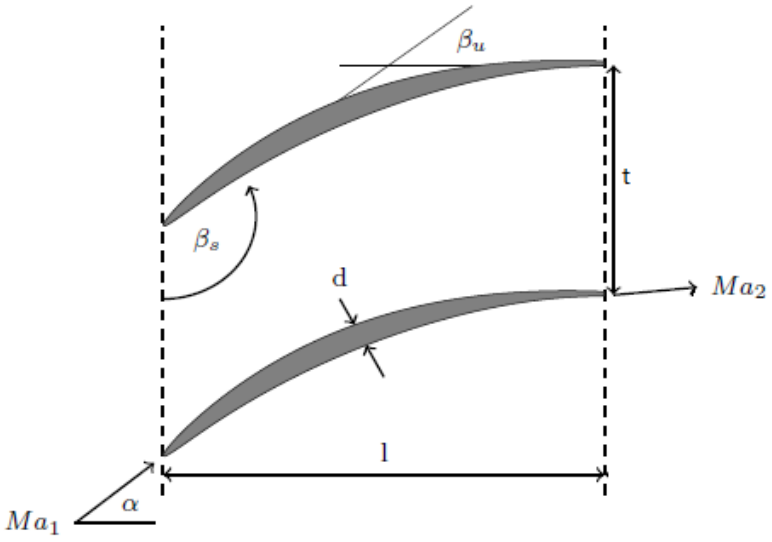

Figure 4.1: Schematic of the NACA 65 V103-220 linear compressor cascade.

Table 4.1: Nominal simulation parameters.

Reynolds number	200,000
$Mach$	0.676
Flow angle α	42°
t	$0.121\,mm$
C	$220\,mm$
C_{axial}	$203,2\,mm$
t/C	0.59
d/C	0.059
β_s	112.5°
β_u	48°
% Tu at LE (pitch average)	1.95%

4.2 LES Numerical Setup

The LES simulation has been performed on one blade-row with 81 791 228 cells, with 83 cells in spanwise (z) direction using 1008 cores. The domain of the LES had pitchwise (y) and spanwise (z) periodic boundary condition, and viscous wall on the blade surface. This setup ensure a non-dependency of the complex flow interactions that end walls and tip leakages cause. The schematic representation of the control domain is shown in figure 4.2. The applied boundaries conditions are shown in Tab. 4.2.

Table 4.2: Boundary condition for the LES.

Inlet boundary conditions	
Absolute Total Pressure	$7138.28\,Pa$
Flow angle	42°
Absolute Total Pressure	$288.15\,K$
Isotropic Reynolds stress	$233.513\,m^2/s^2$
Eddy Length Scale	$0.006\,m$
Outlet boundary condition	
Static Pressure	$6197.73\,Pa$

With respect of producing an appropriate fluctuation field, the synthetic turbulence generator (Shur et al) [49] is used, that was implemented by Morsbach and Franke [34] and tested by Matha et al [32] in TRACE. According to Shur et al [49], the synthetic turbulence generator is based on a set of non-time dependent wave numbers k^n and a prescribed spatial spectrum of the kinetic energy of turbulence represented by a modified von Karman spectrum. Afterwards, the velocity fluctuations are added to the mean velocity

components at the inlet panel of the computational domain. This method is capable of a plausible representation of the anisotropy of the vortical structures, which is an essential feature of near-wall turbulence [49].

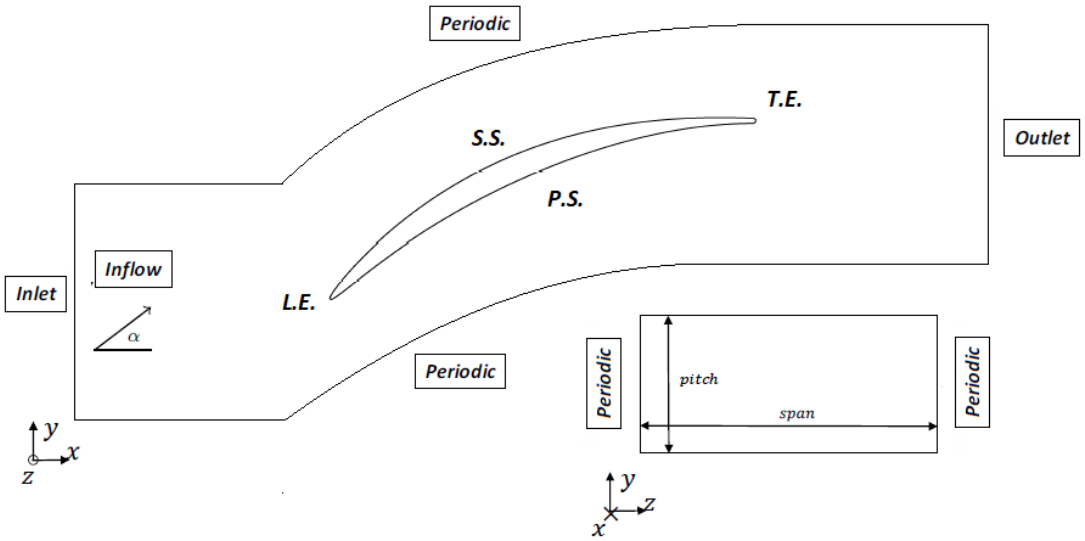

Figure 4.2: Schematic representation of the LES control domain (not to scale).

The simulation was performed by setting the following parameters:

Table 4.3: LES Numerical Setup.

Spatial Discretization	
Scheme	3^{rd} *Upwind*
Limiter	Off
Temporal Discretization	
Scheme	*Explicit Runge Kutta*
Accurancy	3^{rd} *Order*
Boundary condition	
Inlet	*Riemann*
Outlet	$Unsteady - 1D$ *Characteristic*
Wall	$No - Slip$
Turbulence	
Turbulence Treatment	LES
Turbulence Model	WALE
Dimensionless wall-distance	
Wall-normal	< 1
Streamwise	< 45
Spanwise (z)	< 25

As the LES simulations was initialized with a RANS simulations, based on the investigations of Bergmann et al. [5], a statistical averaging of the flow variables took place after the transient phase was completed. This operation was achieved by using $20\,t^*$ through-flow [53] [57], where t^* is defined as:

$$t^* = \frac{C}{U_{axial}}. \tag{4.1}$$

Hereby, C represents the chord length and U_{axial} the in the inlet section. Subsequently, a space averaged has been accomplished along the spanwise direction (z).

4.3 RANS Numerical Setup

In figure 4.3 the RANS simulations control domain is presented. Hereby, one blade-row structured mesh of 997 454 cells is computed with a span length of one cell using 24 cores. The domain is set as periodic boundary conditions in the pitchwise direction (y), symmetry boundary conditions in the spanwise direction (z) and viscous wall on the blade surface

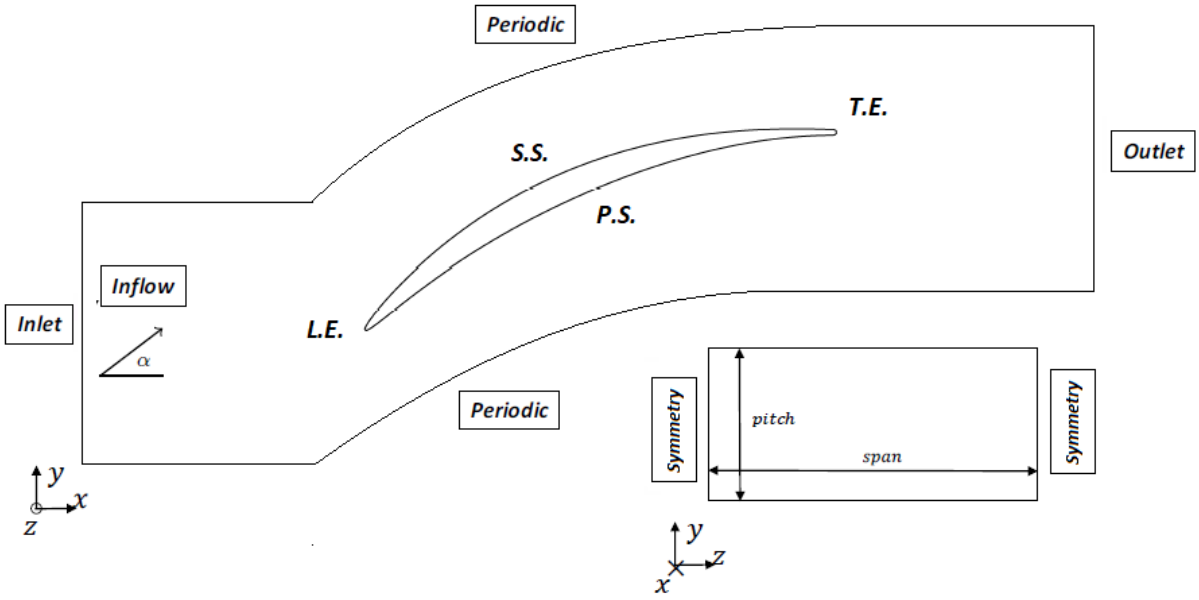

Figure 4.3: Schematic representation of the RANS control domain (not to scale).

The RANS simulations are performed by using the same geometry that is highlighted in the previous section 4.1. Regarding the inlet and outlet boundary conditions, the same thermodynamic values and velocity angles of the LES are set. The turbulence quantities, such as turbulence intensity Tu and eddy length scale L_t, are determined in the section 4.3.2.

The simulations are performed by setting the following parameters:

Table 4.4: RANS Numerical Setup.

Spatial Discretization	
Scheme	*Fromm Scheme*
Limiter	*VanAlbadaSqr*
Temporal Discretization	
Solution Method	*PredictorCorrector*
Boundary condition	
Inlet	*Steady2D*
Outlet	*Steady2D*
Wall	$No - Slip$
Wall-Treatment	*LowReynolds*
Turbulence	
Turbulence Treatment	(U)RANS
Turbulence Model	$Wilcox\ k-\omega$
Stagnation Point Anomaly Fix	*KatoLaunder*
Transition Model	$\gamma - Re_{\Theta}$ *Menter* 2009

4.3.1 Finding suitable boundary condition

The inlet turbulence intensity and eddy length scale play a significant role in the prediction of the laminar-turbulent transition in the boundary layer development [6], as well as overall loss distribution in the wake region. This is due to the fact that different turbulence length scale and eddy length scale lead to different dissipation rates, resulting in significantly altered decay of turbulence intensity in the inlet region.

For a compressible flow, turbulence intensity is defined as:

$$Tu = \frac{u''}{\widetilde{u}} \tag{4.2}$$

with the u'' represents the root mean square (RMS) of the turbulent velocity fluctuations

$$u'' = \sqrt{\frac{1}{3}\left(u_x''^2 + u_y''^2 + u_z''^2\right)} = \sqrt{\frac{2}{3}k}, \tag{4.3}$$

while $\widetilde{u}$ represents the mean velocity field computed using Reynolds-averaged (see section 3.2.1). Nevertheless, turbulence intensity measures the magnitude of the turbulent fluctuations.

On the other hand, eddy turbulence length scale L_t is defined as follows

$$L_t = \frac{\sqrt{k}}{\omega}, \tag{4.4}$$

in which k is the turbulent kinetic energy and ω is the specific dissipation rate.

By setting the turbulence intensity and eddy length scale, the turbulent kinetic energy and the specific dissipation rate in the inlet boundary condition are fixed.

4.3.2 Matching LES Turbulence intensity decay

Within this section, the analysis to find an adequate turbulence inflow is performed to ensure similar operating conditions in regards of the LES data.

In figure 4.5 and 4.6, several simulations are shown. The respective curves represent the evolution of the turbulent intensity in the free stream flow along a centered streamline, as show in figure 4.4.

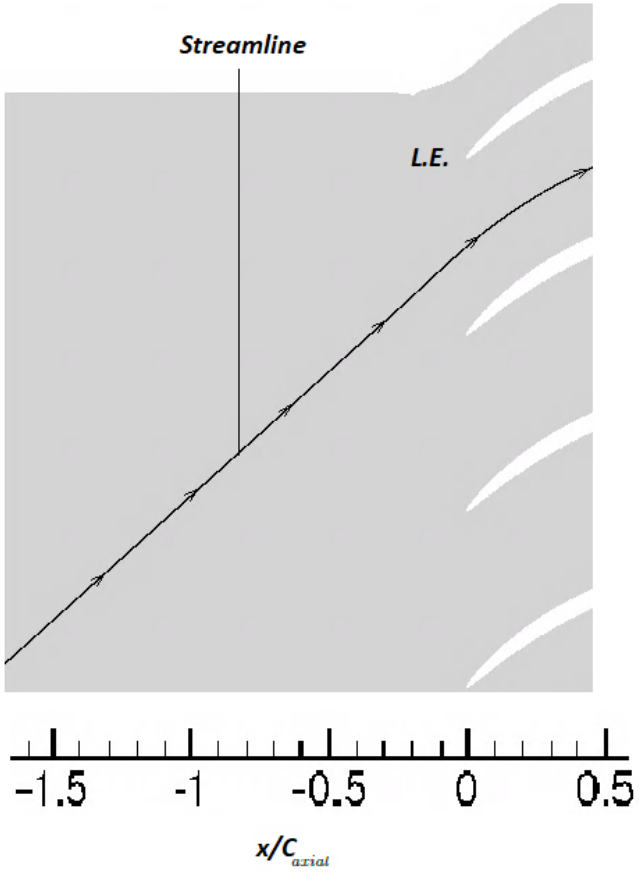

Figure 4.4: Schematic representation of the centered streamline.

In regards of the turbulence intensity decay of the LES, it shows a nonphysical behaviour in the near inlet boundary region, as it drops significantly. The reason is due to the synthetic turbulence generator as it introduces random fluctuations, which size in space and time are dependent on an fitted von Karman spectrum, unlike real turbulence, where a connection between the different velocity components is presented. Therefore, an evolution time (or length) is required before the random fluctuations become physical meaningful fluctuations. As a result, the turbulence values close to the inlet are not taken into account as they do not become meaningful by longer averaging times. Moreover, the blade influences the turbulent intensity slope. As a result, the region of the study is constrained to an interval of -1.4 to -0.5 of the normalized x-coordinate by the axial chord length C_{axial} upstream the leading edge.

In order to match the turbulence intensity of the LES, a study regarding the behaviour of different inlet turbulence intensity and eddy length scale is conducted.

First, the influence of the eddy length scale for a specified turbulence intensity is shown in figure 4.5(a). By setting a lower eddy length scale, the decaying of the turbulent intensity is increased. This is in agreement with the L_t equation (4.4): by fixing the the inlet turbulence intensity Tu, thus the turbulent kinetic energy k, a lower value of the turbulent length scale L_t leads to an greater inlet specific dissipation rate ω and, consequently, a faster degradation of the fluctuations in the free stream.

Afterwards, the influence of changing the inlet turbulence intensity is conducted for a fixed eddy length scale is presented in figure 4.5(b). By fixing the eddy length scale in the inlet region, an higher inlet turbulence intensity leads to greater turbulent kinetic energy introduced in the flow domain and, therefore, higher values of turbulence intensity decay curve.

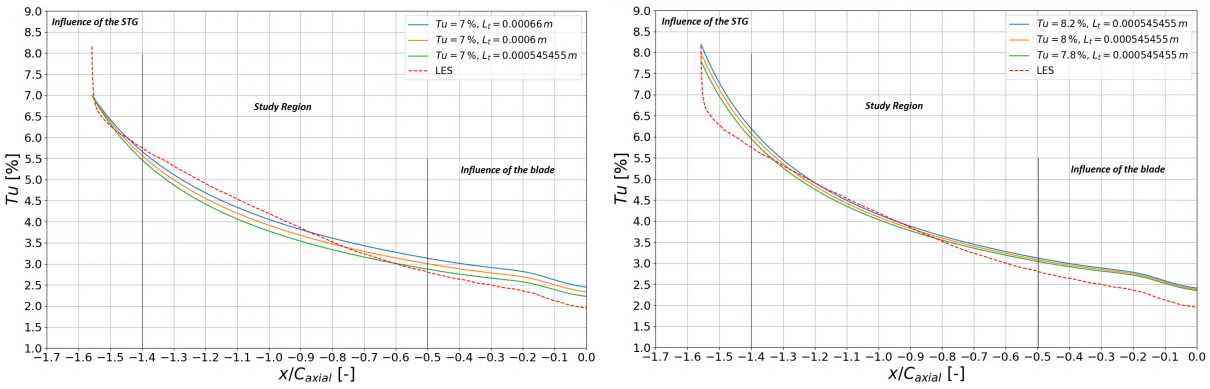

(a) (b)

Figure 4.5: Turbulence intensity decay plotted over the normalized x-coordinate by the axial chord length C_{axial} for constant inlet Tu (a) and constant inlet L_t (b).

The study is further investigated by varying the turbulence intensity and eddy length scale according to the previous observations. Moreover, the viscous blending limiter version 1 and 2 are employed to control the production of turbulent kinetic energy in turbulent flows.

Figure 4.6 show that this extension results in a negligible deviation from the standard eddy viscosity formulation, as the three curves are aligned. The selected parameters that better fit the turbulence intensity decay are shown in figure 4.7. This setup minimize the deviation in regards of the LES turbulence decay in the region of study, and thus ensure similar operating conditions.

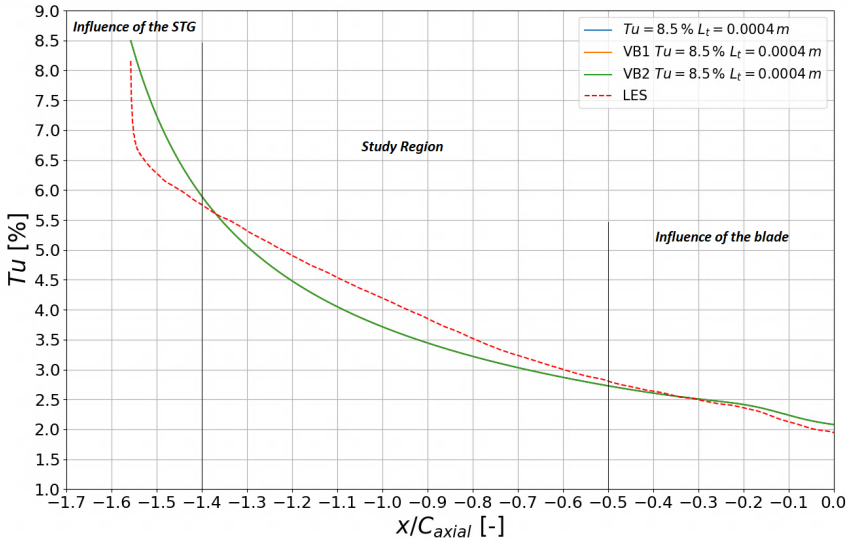

Figure 4.6: Turbulence intensity decay plotted over the normalized x-coordinate by the axial chord length C_{axial} for viscous blending limiter version 1 and 2.

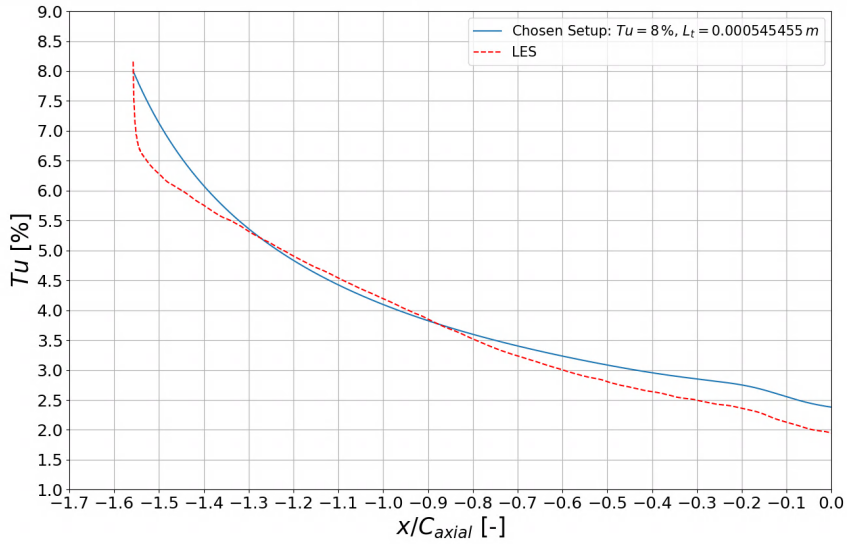

Figure 4.7: Best parameters fit curve of turbulence intensity decay plotted over the normalized x-coordinate by the axial chord length C_{axial}.

4.4 Frozen Approach

Since the aim of this present study is to isolate the behaviour of the $k-\omega$ model in the downstream region of the cascade, the following comparison is conducted by simulating only the wake domain with RANS simulations by using inlet flow properties that derive from the LES data set. Regarding the turbulence quantities, as stressed by many authors, the specific turbulent dissipation rate in RANS simulations is only a variable that aids to reproduce the turbulence kinetic energy field and has no physical meaning for itself [51]. Within a LES context, it has a completely different meaning and values compared to the RANS approach. Hence, a new computation of the specific turbulent dissipation rate ω field needs to be fulfilled. To do so, the "Frozen Approach" is used. This method was first introduced by Parneix [38] in backward-facing step case-study, which consist of isolating the turbulence model by solving the full transport equation for one isolated component of the Reynolds stress tensor and preserve the mean flow field that can be taken from a DNS data base.

Within this research, a similar procedure is used to compute the turbulence transport equation (3.45) for ω in the entire cascade domain, by using the previous turbulence intensity and eddy length scale, and by fixing every flow field variable that arise from the LES data set. Afterwards, a cut is performed to obtain the inlet boundary condition for the wake domain.

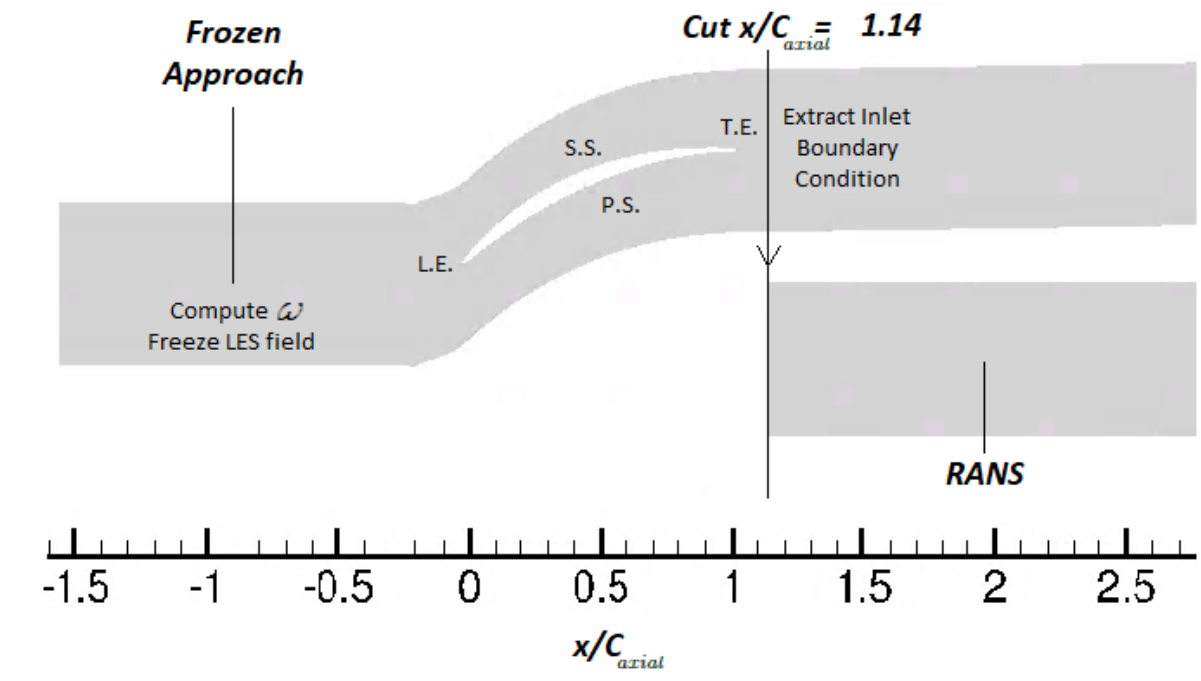

Figure 4.8: Schematic representation of the methodology employed to extract the inlet boundary condition for the wake domain.

In the following chapter, the numerical setup of the wake domain is presented and a grid independence study is conducted.

4.5 Grid Independence Study

The grid convergence study is an important process in verifying that discrete numerical solutions are valid representations of the physic involved in the phenomenon under investigation. Therefore, a grid independence study is performed according to the Fluids Engineering Division of ASME [7]. The total pressure loss distribution as integral value is taken into account to evaluate the discretization error.

4.5.1 Wake Numerical Setup

The respective CFD-simulation model of the wake region is illustrated in figure 4.9. The inlet panel is located at the normalized $x - coordinate = 1.14$ to mitigate the influence of vortex shedding [21], as it is an unstable region. In the inlet panel, the data set that derives from the frozen approach is stored. The domain is set as periodic boundary conditions in the pitchwise direction (y) as well as in the spanwise direction (z). The characteristic measurement cut planes $Cut1.5$ and $Cut2$, which are located at 150% and 200% of the axial chord length, are used in order to analyze the outflow region,

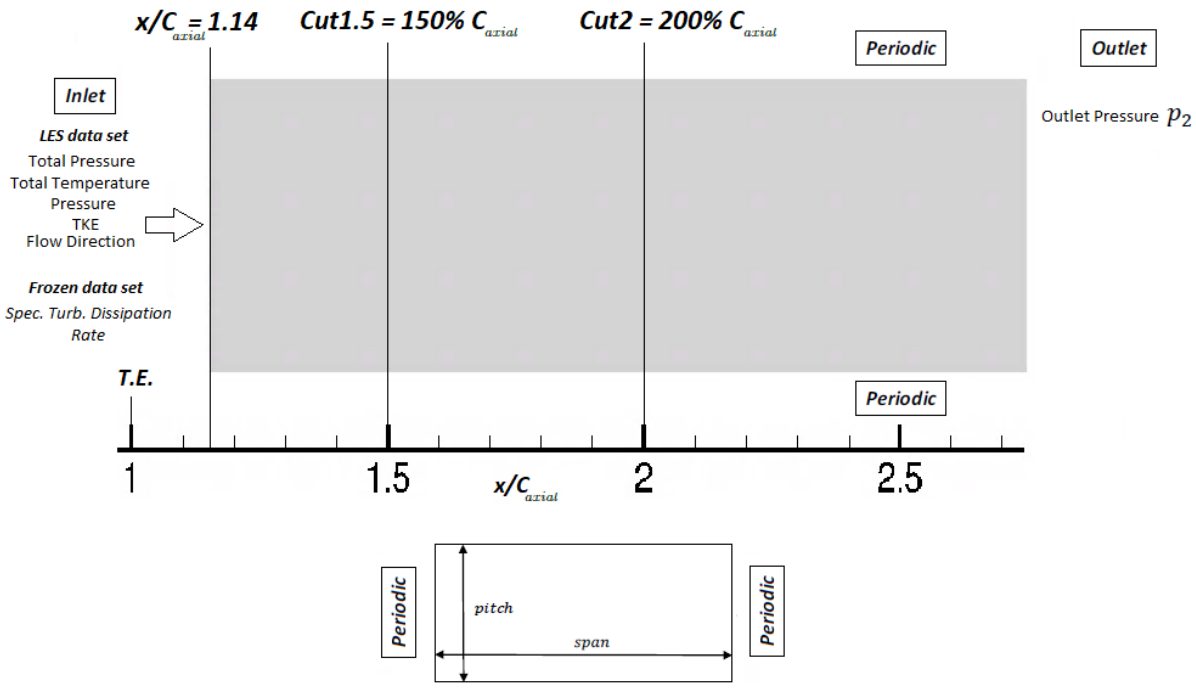

Figure 4.9: CFD simulation model of the wake domain of NACA 65 linear compressor cascade.

The simulations are performed by setting the following parameters:

Table 4.5: Wake Domain Numerical Setup.

Spatial Discretization	
Scheme	*Fromm Scheme*
Limiter	*VanAlbadaSqr*
Temporal Discretization	
Solution Method	*PredictorCorrector*
Boundary condition	
Inlet	*Riemann*
Outlet	*Steady2D*
Turbulence	
Turbulence Treatment	(U)RANS
Turbulence Model	*Wilcox* $k-\omega$
Stagnation Point Anomaly Fix	*KatoLaunder*

4.5.2 Grid Refinement Setups

According to the Fluids Engineering Division of ASME [7], three significantly different sets of grids are selected. For each grid, the representative grid size h is determined as:

$$h = \left[\frac{1}{N}\sum_{n=1}^{N}\Delta V_i\right]^{\frac{1}{3}}. \tag{4.5}$$

As suggested by the Grid Convergence Method [7], the grid refinement factor r, which is defined as

$$r = \frac{h_{coarse}}{h_{fine}}, \tag{4.6}$$

should be greater than 1.3 based on experience. The following table resume the chosen parameters within this case study:

	Coarse(3)	Average(2)	Fine(1)
Grid Size h	$6 \cdot 10^{-4}$	$3 \cdot 10^{-4}$	$2.1 \cdot 10^{-4}$
N. of Cells	113 524	452 972	925 656
Grid Refinement Factor r_{21}	1.42		
Grid Refinement Factor r_{32}	2		

Table 4.6: Selected sets of Grids.

The number of cells is referred to a domain with a span length of one cell and equidistant grid, meaning that the cells in x-y plane have the same length and no refinements are performed in areas with high gradients. It has been found out that TRACE solver [29] does not properly work within this test case, as it created a significant velocity component along the spanwise direction (z) for symmetric boundary condition, thus invalidating the results. To fix the problem, a refinement of 9 cells along the spanwise direction (z) has been achieved using periodic boundary conditions.

4.5.3 Wake Analysis

As key variable important to the objective of the study, the total pressure loss distribution is considered in regards of the characteristic measurements cut planes. Within this thesis, the total pressure loss is quantified by the total pressure loss coefficient ω_{loss}, which is defined as

$$\omega_{loss} = \frac{P_{t,1} - P_t}{P_{t,1} - P_1} \tag{4.7}$$

with the inlet total pressure $P_{t,1}$, the static pressure at the inlet position P_1 and the total pressure P_t at the location of interest. The pressure loss distribution in the wake domain, along the normalized y-coordinate, is presented in figure 4.10 for both characteristic planes at $Cut1.5$ and $Cut2$.

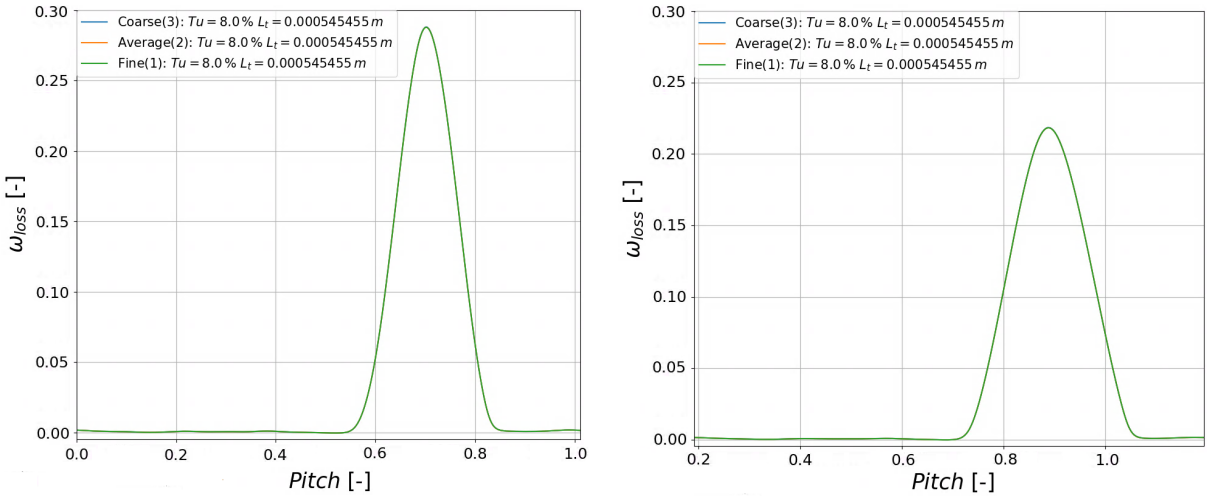

(a) $Cut1.5$ (b) $Cut2$

Figure 4.10: Grid indipendence study: Pressure loss distribution over pitch (y/t) in the wake region for the different grid cases.

It is evident that the grid convergence is achieved, as the total pressure loss coefficient is aligned for every set of grid. Hereby, it is to mention that the outflow angles of all grid

cases do not show significant deviations. According to the Grid Convergence Method, the error estimates are presented in tab, that are computed with the Richardson extrapolation (RE) method [44] [46], along with the apparent order p. The total pressure loss coefficient in integral values are taken into account to extrapolate these error estimates.

Table 4.7: Error estimates values for the Cut planes at 150% and 200%.

	Cut plane at 150%			**Cut plane at 150%**		
	Coarse(3)	Average(2)	Fine(1)	Coarse(3)	Average(2)	Fine(1)
ω_{loss}	0.045091	0.045094	0.045096	0.043689	0.043691	0.043692
p	3.65			0.44968		
ϕ_{ext}^{21}	0.0451			0.043697		
e_a^{21}	0.0045			0.002152		
e_{ext}^{21}	0.00169			0.012373		
GCI_{fine}^{21}	0.00211			0.015469		

The table supports the evidence that the medium size grid delivers sufficient grid independent results since the approximate relative error remains below 1% in total pressure loss. Furthermore, in figure 4.11 is visualized the grid convergence where the extrapolated value, which is the expected value for a finer grid, clearly shows that all the convergence criteria are matched. Therefore, the medium size grid provides adequate results and it is adopted as a valid representation within the following comparison with the LES simulation.

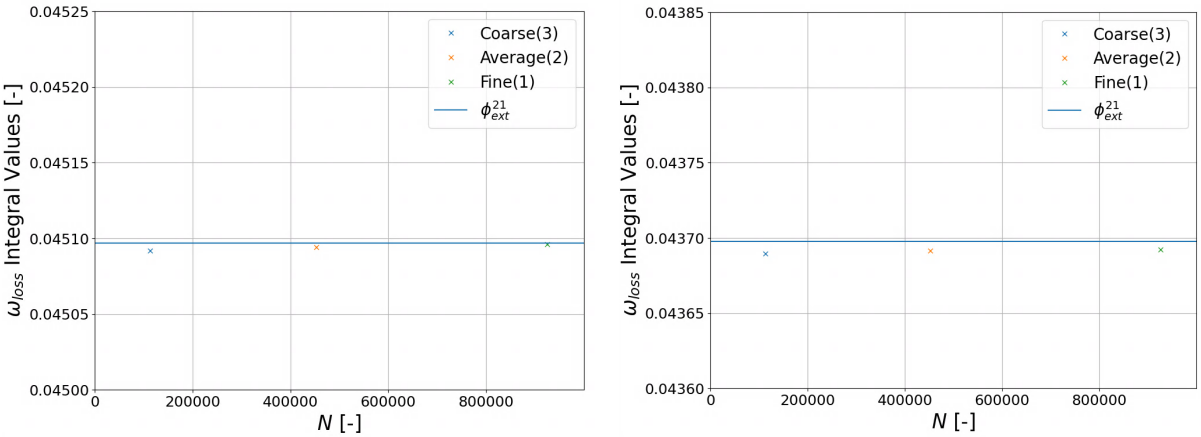

(a) $Cut1.5$ (b) $Cut2$

Figure 4.11: Grid convergence curve: total pressure loss coefficient ω_{loss} in integral values over total number of cells N for the different grid cases.

4.5.4 Influence of the Prescribed Inflow Turbulence

Within this section, the sensitivity of employing different inlet turbulence intensity and eddy length scale is conducted in regards of the total pressure loss coefficient ω_{loss}.

The RANS simulations used within this case are shown in figure 4.12. The "frozen" setup is the simulation that ensure the best fit in regards of the turbulence intensity decay of the LES. The "frozen2" setup is chosen as it overestimates the turbulence intensity decay, while the "frozen3" setup is used as it predicts a slower turbulence intensity decay compared to the "frozen" setup. Figures 4.12(a) and 4.12(b) show the pressure loss distribution in the wake domain along the normalized y-coordinate for both characteristic cut planes. Results show that small deviations of inlet turbulent intensity and eddy length scale do not affect the total pressure loss distribution as the slopes are aligned for the three cases.

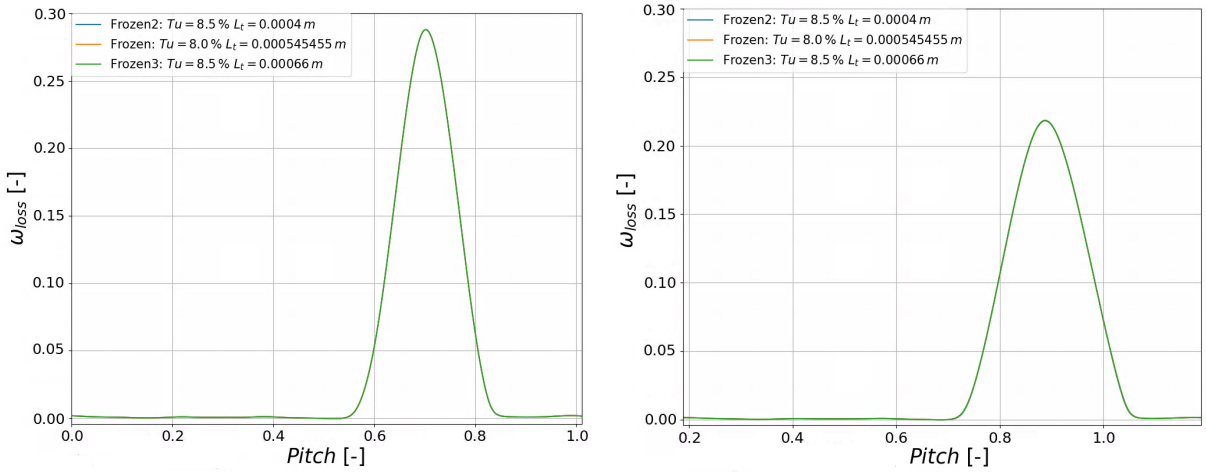

(a) $Cut1.5$ (b) $Cut2$

Figure 4.12: Inflow turbulence sensitivity: total pressure loss coefficient ω_{loss} over pitch (y/t) in the wake region for the different grid cases.

5 RANS-LES Results Comparison

In the following, the comparison is conducted between RANS and LES simulations. Regarding RANS, the simulation in which $Tu = 8\,\%$ and $L_t = 0.000545455\,m$ is taken into account as the inflow turbulence intensity decay minimize the deviation with the LES one. The study focuses on the total pressure loss coefficient ω_{loss}, the strain rate tensor E_{ij}, the Reynolds stress tensor τ_{ij} and its anisotropy in the wake region. The goal of this comparison is to highlight the limitations and performance of the RANS simulation in regards of the turbulence quantities and to provide a possible outlook for the development of appropriate RANS model extensions or analysis.

5.1 Total Pressure Loss

As the total pressure loss is a critical parameter in turbomachinery design, figs. 5.1(a) and 5.1(b) compare the wake profiles by LES and RANS for the two characteristic measurement cut planes.

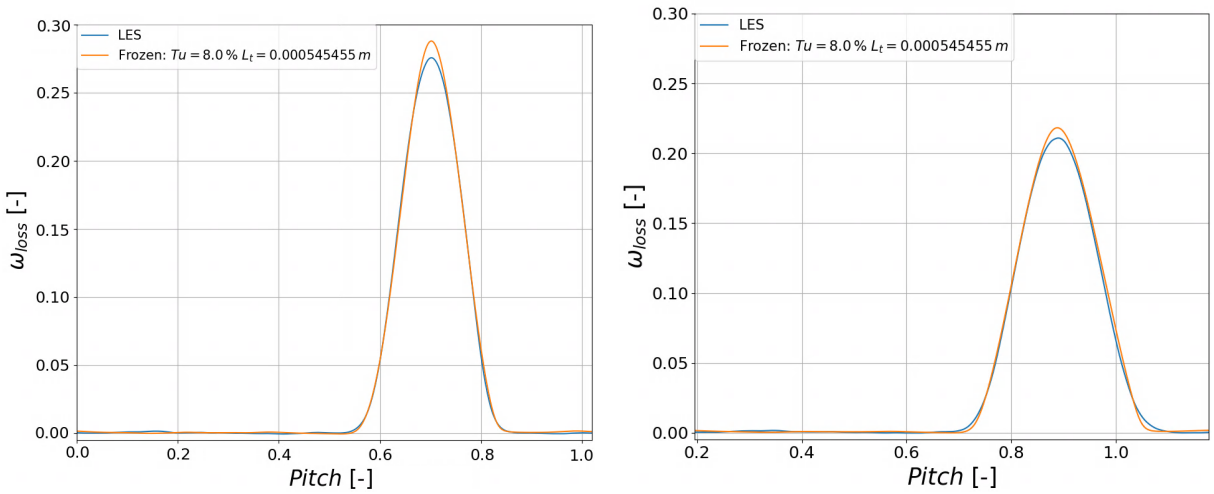

(a) $Cut1.5$ (b) $Cut2$

Figure 5.1: Total pressure loss coefficient over pitch (y/t) in the wake region for the LES (Blue color) and RANS (Orange color).

Generally, the LES predicts wider wakes compared to the RANS, while the latter tend to estimate a deeper total pressure deficit [27]. Within this research, as shown in figure 5.1, the RANS predicts a deeper wake loss peak for both cut planes compared to the LES.

Regarding the total pressure loss coefficient distribution at $Cut1.5$ of the chord length,

the RANS simulation matches the LES wake width, mainly at the suction side, but exhibits a higher peak deficit in the total pressure loss coefficient distribution. As the wake progresses towards the outlet, at the second location, the RANS simulation predicts a narrower wake compared to the LES case. A slightly lower deviation between the peaks deficiencies between the RANS and the LES is presented compared to the previous location.

Moreover, figure 5.2 displays the integral values of the total pressure loss coefficient for both cut planes. The greater deviation at the second location suggests that the mixing out of the wake in the LES case is faster than in the RANS simulation.

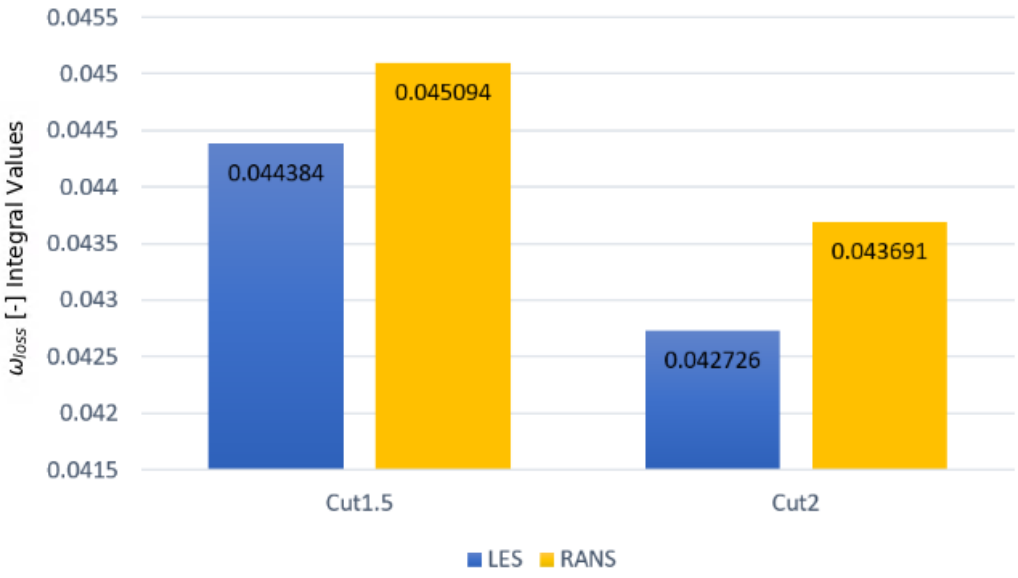

Figure 5.2: Integral values of the total pressure loss coefficient ω_{loss} for the LES (Blue color) and RANS (Orange color).

Despite the highlighted differences, the RANS performs well enough in predicting the total pressure deficiencies.

5.2 Strain Rate Tensor

The strain rate tensor $\widetilde{E_{ij}}$ emerges in the mean viscous stress tensor $\overline{\sigma_{ij}}$ and in the Reynolds stress tensor τ_{ij} in the RANS equations (3.33). As both terms are responsible of the change in mean momentum and energy of a fluid element, the strain rate tensor is analysed in depth since it may play a role in the deviation of the total pressure losses in the wake region compared with the LES.

The strain rate tensor describes the rate of change of the deformation of a molecule and

it consists of a symmetrical matrix of six components. The strain rate tensor is rotated with respect to the mean outflow angle of the wake, so as to proceed the analysis within a streamwise Cartesian coordinate system, that is shown in figure 5.3.

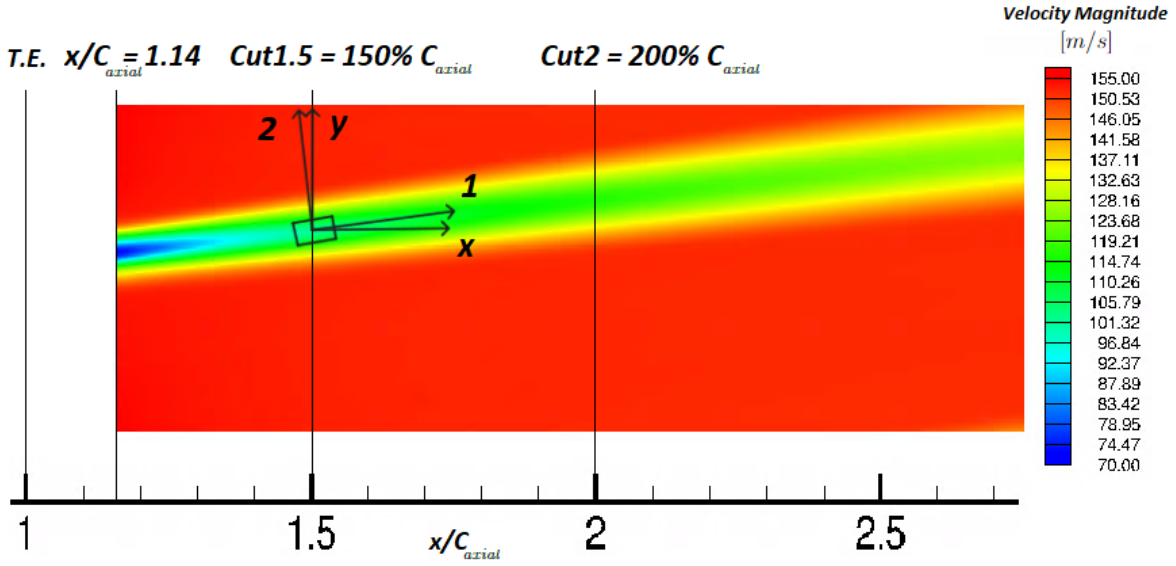

Figure 5.3: Coordinate rotation over the velocity magnitude contour plot of the RANS simulation.

As the velocity field along the principle axis 3 is negligible, the three components of the principle strain rate tensor are

$$\widetilde{E_{3j}} \approx 0, \tag{5.1}$$

therefore, they are not considered within this analysis.

In fig. 5.4 and 5.5 the comparison of the strain rate tensor between the LES and RANS is presented for both cut locations, where the pressure side (P.S.) and the suction side (S.S.) are taken into account for the analysis.

The $\widetilde{E_{11}}$ component is analyzed at the $Cut1.5$ position (fig. 5.4(a)), in which the RANS simulation matches the slope of the LES. However, a small deviation is observable at the pressure side location. At the second cut plane $Cut2$ (fig. 5.5(a)), the RANS simulation shows a good alignment with the LES curve at the pressure side location. Nevertheless, the behaviour of the first component it is not fully captured by the RANS at the suction side location, as the RANS shows a narrower strain rate component compared to the LES.

The second component $\widetilde{E_{22}}$ is taken into account for both location. It is observable a similar trend in respect of the previous component $\widetilde{E_{11}}$. The RANS manifests a slightly higher peak at the pressure side location for the first cut plane (figure 5.4(b)). On the

other hand, at the suction side location along the Cut2 (figure 5.5(b)), the RANS is not able to properly predict the decay of the LES.

Finally, the shear strain $\widetilde{E_{12}}$ component is also considered (figure 5.4(c)). At the first cut location, a good alignment between both simulation is recognizable. As for the previous components at the second cut plane (figure 5.5(c)), the suction side location is not fully matched by the RANS, with a slightly lower peak compared to the LES.

Within this analysis, the $k-\omega$ model shows good alignment with the LES results, showing only minor discrepancy between the slope of the LES wake decay at the suction side location. The analysis is extended in regards of the Reynolds stresses in the following chapter.

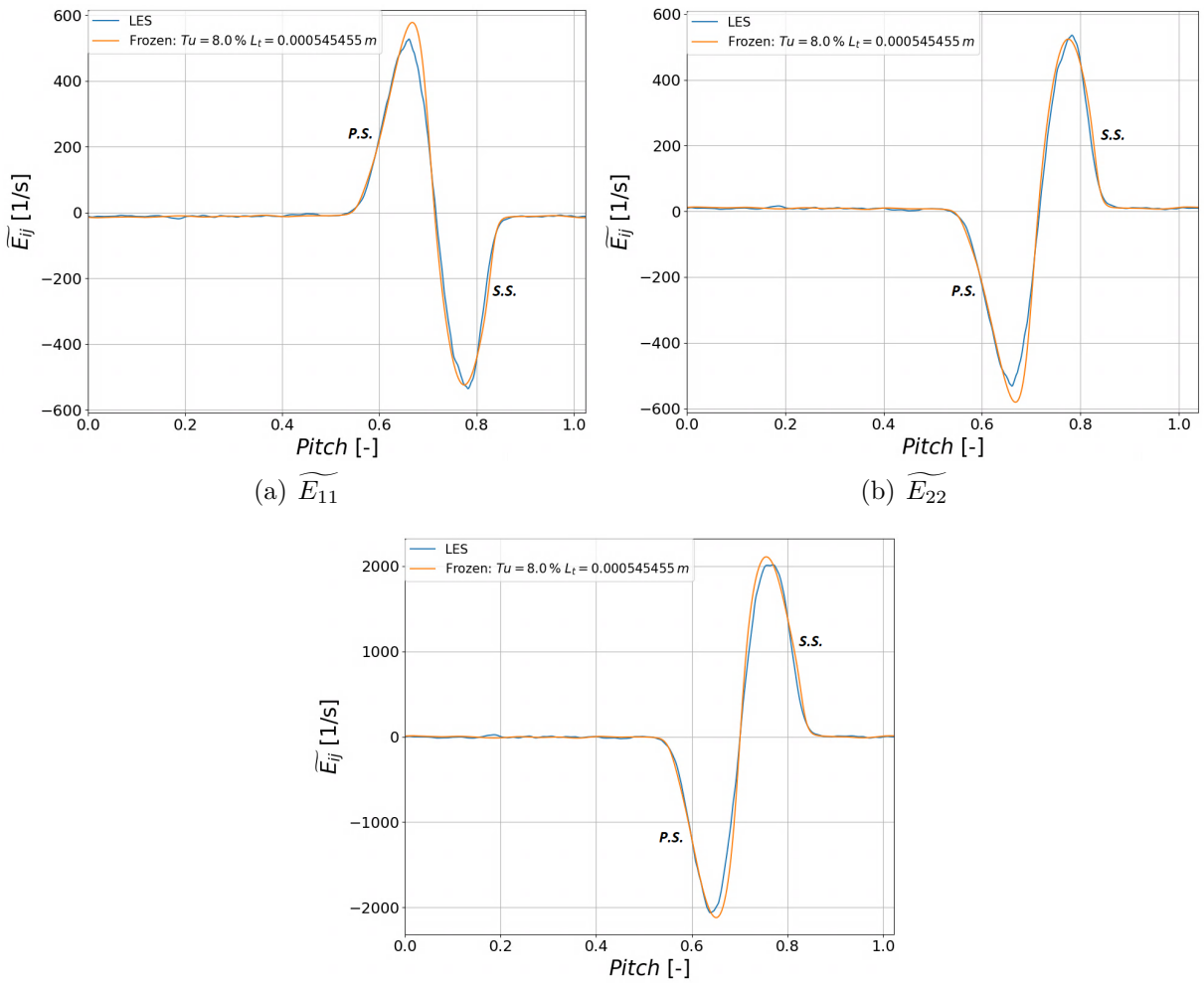

(a) $\widetilde{E_{11}}$ (b) $\widetilde{E_{22}}$

(c) $\widetilde{E_{12}}$

Figure 5.4: Strain rate tensor components over pitch (y/t) in the wake region at 150% of the axial chord length for the LES (Blue color) and RANS (Orange color).

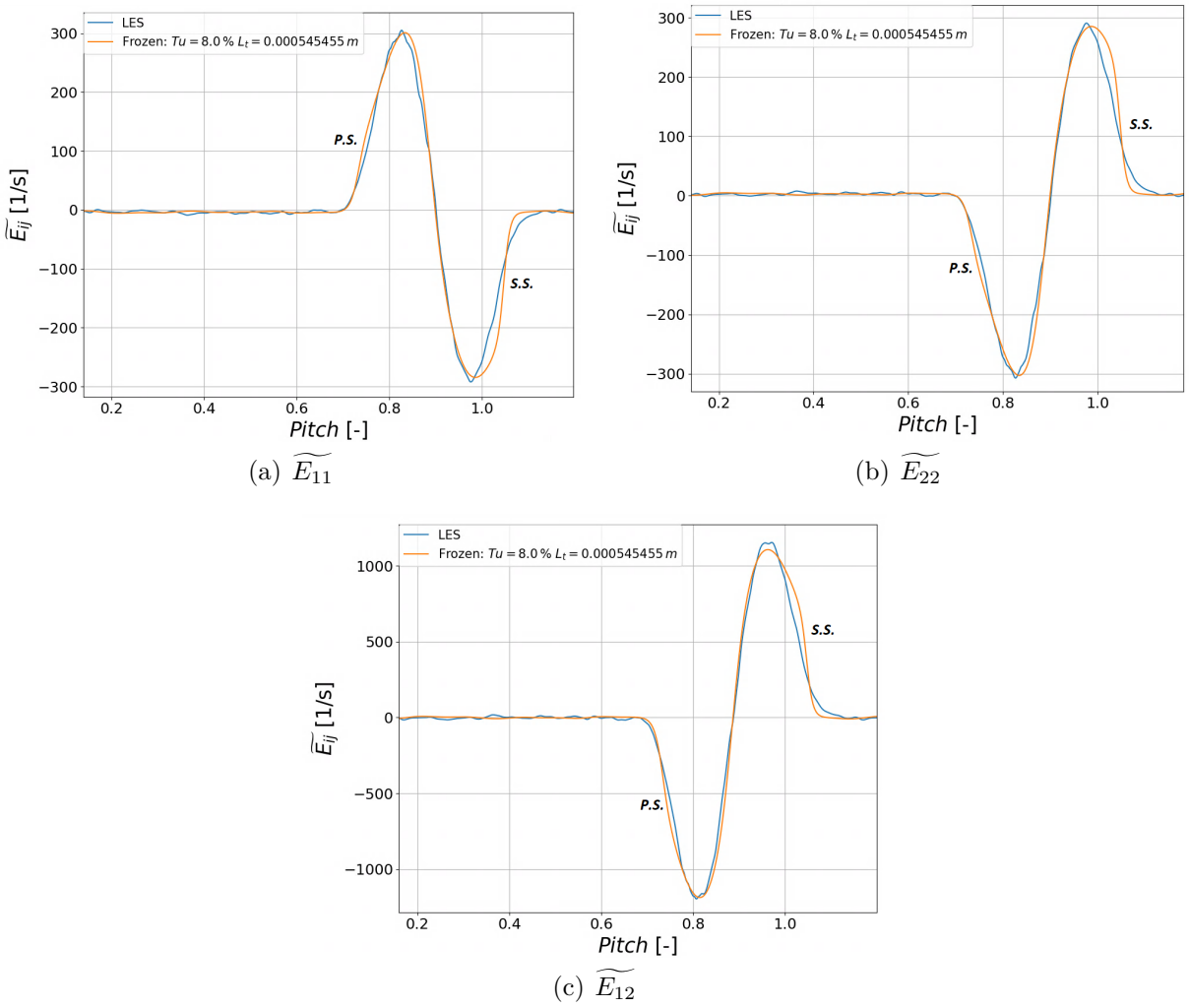

(a) $\widetilde{E_{11}}$ (b) $\widetilde{E_{22}}$

(c) $\widetilde{E_{12}}$

Figure 5.5: Strain rate tensor components over pitch (y/t) in the wake region at 200% of the axial chord length for the LES (Blue color) and RANS (Orange color).

5.3 Reynolds Stress Tensor

As the Reynolds stress tensor can be related to the total pressure (Bear et al. [3]), the presenting chapter aims to provide a linkage between these two key variables in a turbulent flow. The Reynolds stress tensor appears after the averaging process and it describes the turbulent contribution to the mean flow, thus the change in mean momentum and energy of a fluid particle equation (3.33). As for the strain rate tensor, the Reynolds stress is rotated in respect of the mean outflow angle of the wake. The figures 5.6 and 5.7 compare the diagonal Reynolds stress components $\widetilde{u_i'' u_i''}$ of LES and RANS at 150% (Cut1.5) and 200% (Cut2) of the axial chord length.

First, the $\widetilde{u_1'' u_1''}$ component is taken into account at the first cut plane (figure 5.6(a)). As for the total pressure loss, the RANS shows a narrower curve with a slightly lower peak at

the pressure side location. As the wake progresses downstream to the second cut plane, a greater deviation from the LES is observed, as illustrated in figure 5.7(a). Despite this, the RANS does perform well in regards of the LES.

Second, the $\widetilde{u_2''u_2''}$ component shows a significant deviation between the two cases in Cut1.5 (figure 5.6(b)). While the LES shows one peak at the pressure side location, the RANS predicts two peaks, with a much greater peak values at the suction side location that contributes in increasing the total pressure losses. This behaviour is maintained in the Cut2 (figure 5.7(b)), with a narrower wake spread compared to the LES.

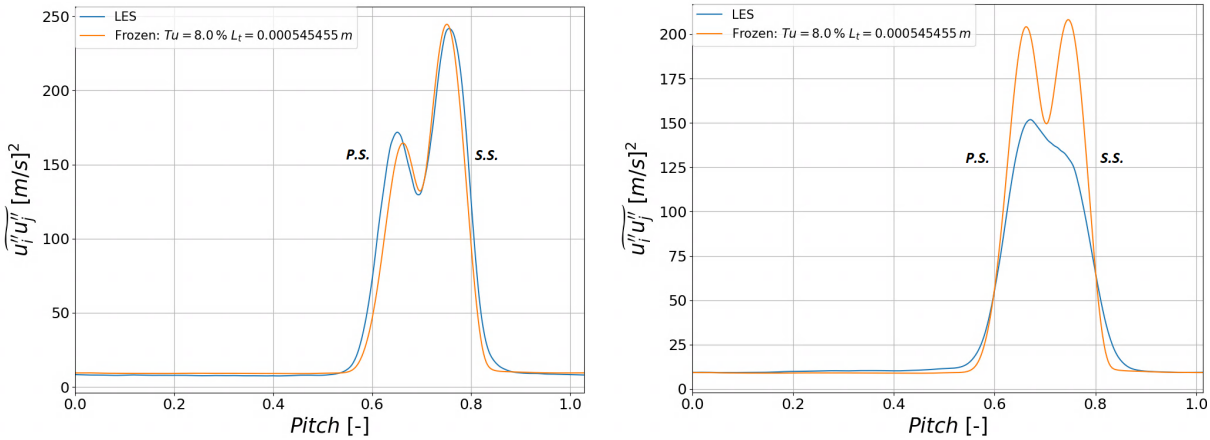

(a) $\widetilde{u_1''u_1''}$

(b) $\widetilde{u_2''u_2''}$

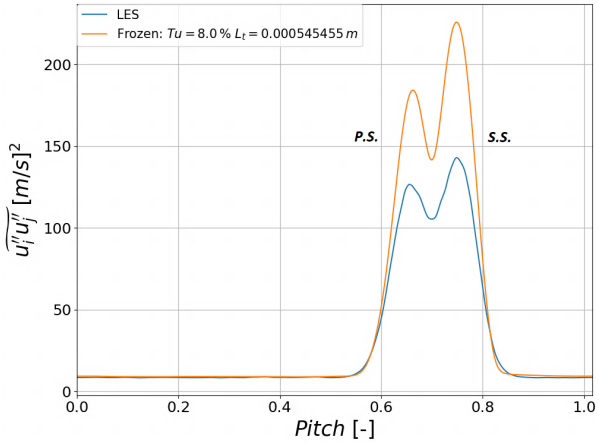

(c) $\widetilde{u_3''u_3''}$

Figure 5.6: Diagonal Reynolds stress tensor components over pitch (y/t) in the wake region at 150% of the axial chord length for the LES (Blue color) and RANS (Orange color).

Finally, the third component $\widetilde{u_3''u_3''}$ highlights the fact that even if the case study is two-dimensional, eddies are unsteady and three-dimensional as this components has significant values compared to the others. While the wake width is well-matched, the RANS simulation over-predicts the values that arise from LES for both peaks. At the second location

(figure 5.7(c)), the deviation between the two peaks persists and a narrower curve is predicted by the RANS simulation.

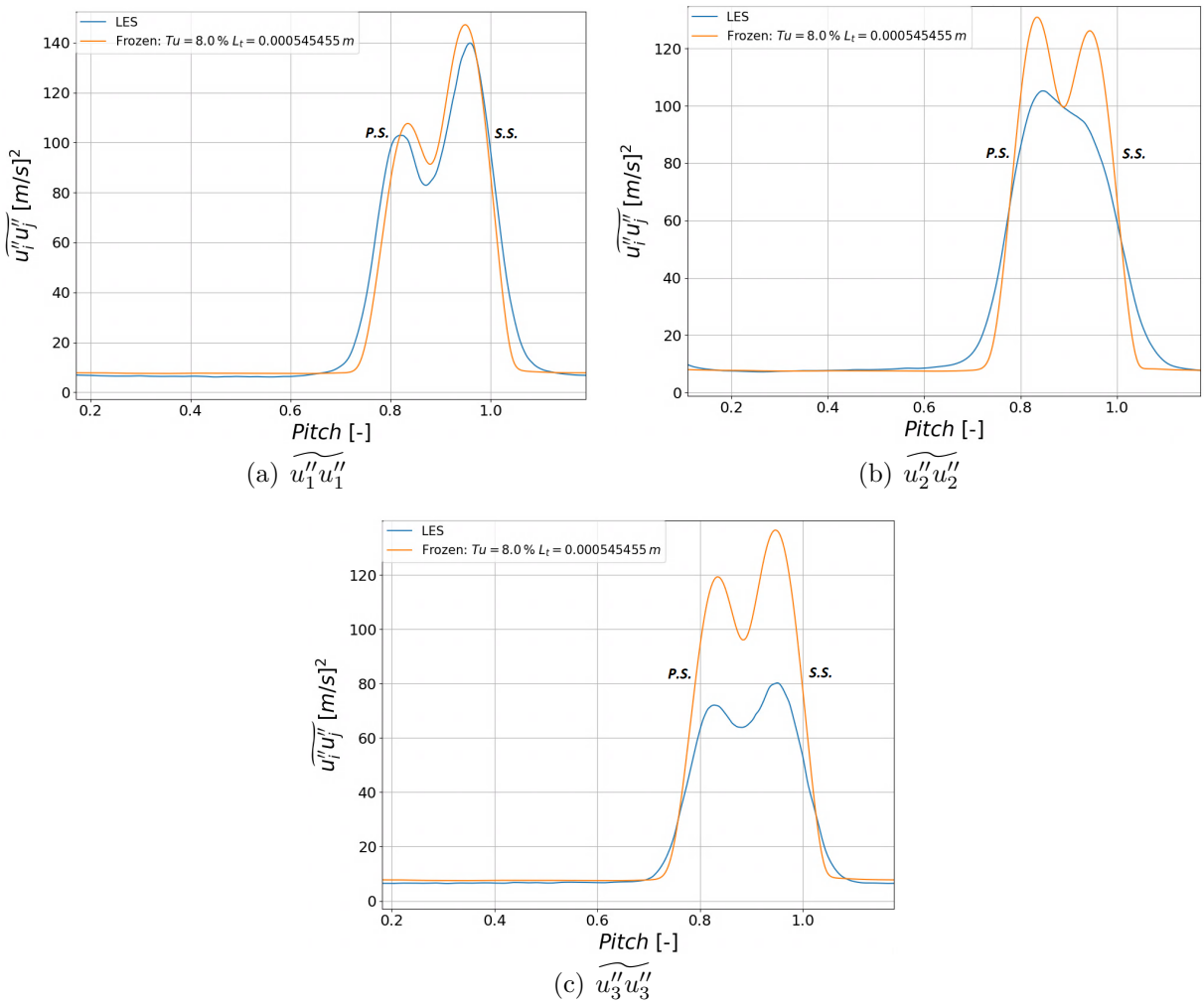

(a) $\widetilde{u_1''u_1''}$ (b) $\widetilde{u_2''u_2''}$

(c) $\widetilde{u_3''u_3''}$

Figure 5.7: Diagonal Reynolds stress tensor components over pitch (y/t) in the wake region at 200% of the axial chord length for the LES (Blue color) and RANS (Orange color).

The Reynolds stress component $\widetilde{u_1''u_2''}$ is now taken in consideration in figure 5.8, as it arises due to the existence of a mean velocity gradient. In this scenario, the transversal fluctuations components feed the fluctuations that are aligned with the mean flow and so in the other way around, leading to a phenomenon that amplifies the fluctuations in the fluid flow. Along the Cut1.5, a significant deviation is presented, with the RANS simulation predicting a lower peak at the pressure side location and a higher peak at the suction side location compared to the LES. This trend is maintained at the second cut location, showing a narrower curve spread. Furthermore, the LES captures the component in the outer wake region, while the RANS fails to predict it. The reason is due to the applied inlet boundary condition, as the turbulence kinetic energy k and specific turbulent dissipation rate ω are the only turbulence quantities that are given, while no information are provided in regards of the Reynolds stresses.

The two components $\widetilde{u_1''u_3''}$ and $\widetilde{u_2''u_3''}$ are negligible compared to the previous components and therefore not considered.

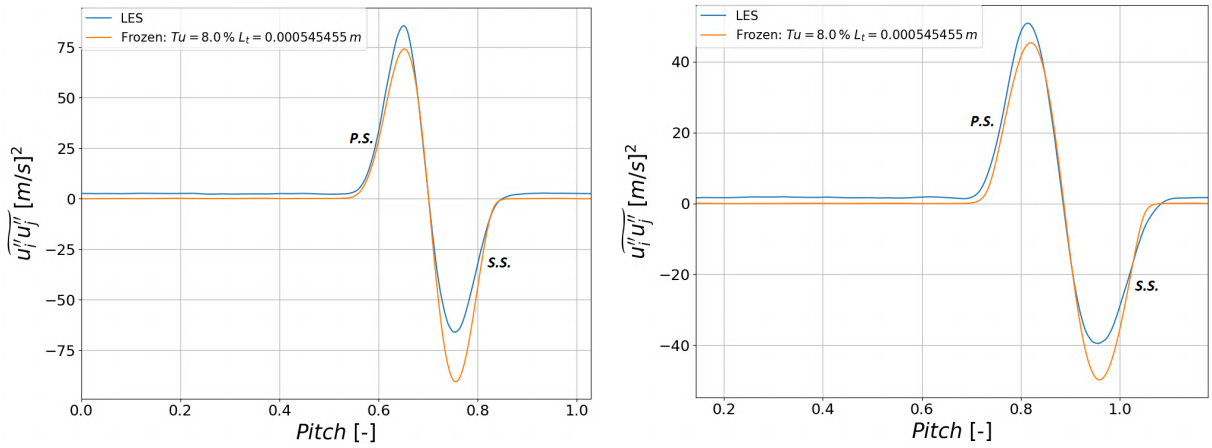

(a) $Cut1.5$ (b) $Cut2$

Figure 5.8: Non-diagonal Reynolds stress tensor component $\widetilde{u_1''u_2''}$ over pitch (y/t) in the wake region for the LES (Blue color) and RANS (Orange color).

5.4 Reynolds stress anisotropy

To get a better overall understanding of the turbulence state and its development in the wake region, figure 5.9 shows the componentality contours of the LES cascade. Afterwards, the comparison of the wake domain is presented between RANS and LES in figure 5.10(a) and 5.10(b), respectively. To do so, the methodology of Emory and Iaccarino (2014) [12] is used, by mapping the weights C_{ic} of the barycentric map to the RGB channels.

In figure 5.9, the LES inflow is characterized by an isotropic 3C turbulence state, indicated by blue color, which is consistent with the applied turbulent boundary conditions (STG). As the flow enters the passage, a shift from an isotropic 3C state to a slightly more 2-component turbulence flow (darker blue) is presented because of the imposed curvature. Within compressor application, the fluid flow is decelerated in the passage, implying that the mean velocity gradient does not promote the production and the redistribution of the turbulent fluctuations, as in turbine applications (Fard Afshar, Deutsch et al [2]).

At the leading edge, the redistribution effect of the incoming freestream 3C isotropic turbulence (Xiong and Lele, 2007)[56] leads to 2C region directly above the 1C layer next to the wall, mainly at the suction side of the blade (green color, region ①). The boundary layer is dominated by 1C component, highlighted by the red color. The 1C layer spans from near leading edge to the separation point, where a redistribution of the fluctuations is detectable near the trailing edge, indicated by the green color (region ②).

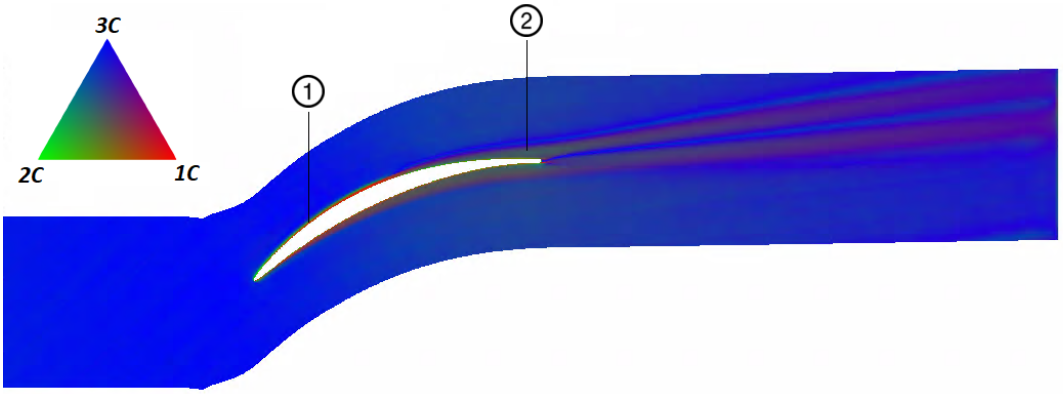

Figure 5.9: Componentality of Reynolds stress anisotropy tensor for the LES cascade.

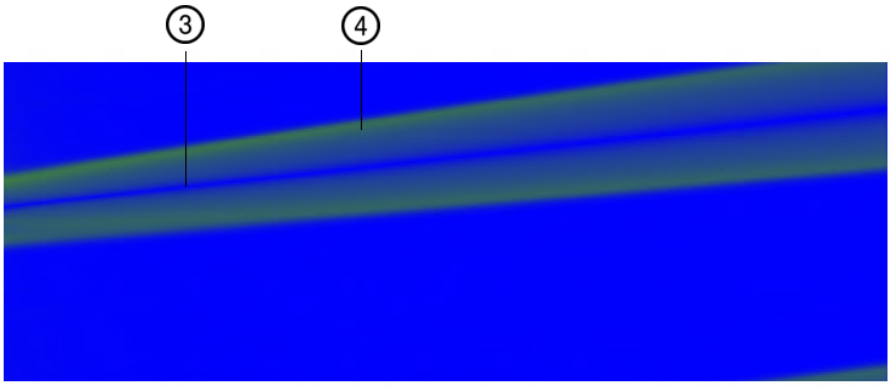

(a) RANS

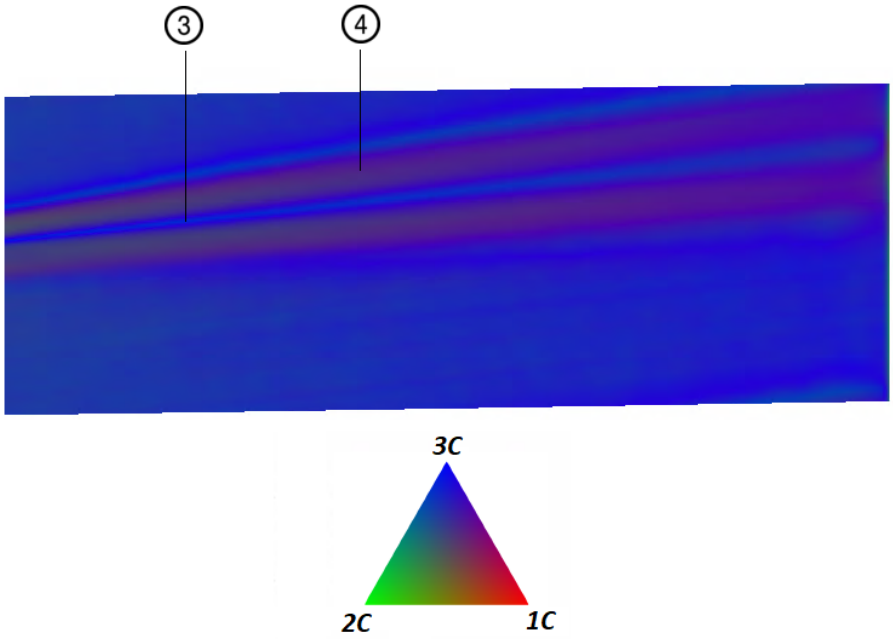

(b) LES

Figure 5.10: Componentality of Reynolds stress anisotropy tensor in the wake domain for the RANS (a) and LES (b).

In figure 5.10 the comparison is illustrated. It is observable that the RANS simulation fails to predict the redistribution of the 3C isotropic component of the freestream. This is consistent with the previously analyzed Reynolds stress component $\widetilde{u_1'' u_2''}$, as the RANS does not fully capture the two fluctuation components in the freestream (figure 5.10(a)).

The center wake area (region ③) is characterized by 3C turbulent state. Within the LES, the center wake is wider compared to the RANS simulation. This is in agreement with the total pressure loss distribution, as the RANS simulation predicts a narrower and greater peak, in contrast with the LES.

Another area of interest is the zone ④ as it is directly connected to the boundary layer development. By moving along the perpendicular direction of the the streamwise direction from the center wake towards the freestream region, the LES shows a blue color that shifts towards a darker blue, promoting a shift to a more anisotropic 2 component. Subsequently, the separation layer leads to a greater 2C turbulence state, that is consistent with the previous analyzed region ②. The isotropy is reinstated once the wake encounters the freestream. As the wake progress further downstream, the anisotropy switches to a lighter blue due to the mixing out of the wake with the freestream. On the other hand, the RANS simulation predicts a significant 2C turbulence state shift (yellow-green color) from the isotropic 3C turbulent, especially near the outer wake region, and it is maintained towards the outlet. Hence, it is consistent with the total pressure loss distribution, along with the Reynolds stress tensor, as the decay of the wake is slower compared to the LES.

6 Conclusion and Future Work

The work presented here focuses on the performance of RANS turbulence model regarding the mixing process of the turbulent wake flow of an high-pressure-compressor cascade. Hereby, the results have been compared with an high fidelity data LES simulation. In order to compare and evaluate the RANS results, an inlet boundary condition study has been conducted to find an adequate turbulence inflow, and thus ensure similar operating conditions in regards of the LES data. Afterwards, the "Frozen approach" has been employed for computing the ω transport equation and by preserving the LES flow field. This operation has been carried out to extract the inlet panel for the wake domain. A grid independence study has been performed in order to provide adequate result validations. Consequently, the influence of the prescribed inflow turbulence has been studied, showing that different turbulent intensity and eddy length scale only affect the total pressure loss peak by a negligible deviation. The comparison between the RANS and LES simulations is conducted by analyzing and relating the turbulence quantities with the total pressure losses distribution. The investigation reveals that RANS agrees well with the total loss trends shown by the LES, exhibiting only minor discrepancy in the center wake and on the curve width, but not in an extent that would compromise the design processes. Moreover, the strain rate tensor has been analyzed within a streamwise Cartesian coordinate system, showing that the RANS is able to capture every component, despite a small variation in predicting the slope at the suction side location as the wake develops further downstream. The analysis has been extended in regards of the Reynolds stresses. Results show that the RANS simulation is able to predict the first diagonal component of the Reynolds stress tensor according to the LES, but it fails to accurately reproduce all the others. Mainly, the $\widetilde{u_2''u_2''}$ and $\widetilde{u_3''u_3''}$ are responsible for the deviation of the total pressure loss distribution between the RANS and LES simulations. On one hand, the RANS simulation predicts a double peak curve in regards of the $\widetilde{u_2''u_2''}$ component, while the LES shows only one peak. On the other hand, the $\widetilde{u_3''u_3''}$ is significantly over-estimated by the RANS simulation. To get a better overview of the Reynolds stress tensor, its anisotropy has been visualized with the the Emory and Iaccarino (2014) color map assignment applied on the baricentric map of Banerjee et al. (2007). The RANS simulation shows a significant 2C turbulence state, especially in the wake region near the freestream, that is conserved towards the outlet, while the LES detects a 2C turbulent state that shifts to a more 3C isotropic state as the wake develops along the streamwise direction.

In conclusion, the $k-\omega$ model is capable of predicting the total pressure loss and the strain rate tensor, thus the mean viscous stress tensor. On the contrary, the turbulence state shows discrepancies with the LES and it is not able to accurately reproduce the Reynolds stress tensor and its anisotropy. Therefore, the small deviations in the mixing out of the wake and total pressure loss distribution are likely connected to the differences in the Reynolds stresses.

This research opens to the possibility of investigating the wake by using the Reynolds

stress transport models or the explicit algebraic Reynolds stress models (EARSM) and compare the results with the standard $k-\omega$ model. Moreover, the present study provides a possible guidance for future model extensions of standard eddy viscosity models, as it highlights the main deficiencies of the model in reproducing proper turbulent topology in the wake region.

Bibliography

[1] Adamczyk, John J.: Wake mixing in axial flow compressors. In: *Turbo Expo: Power for Land, Sea, and Air* Bd. 78729 American Society of Mechanical Engineers, 1996, S. V001T01A002

[2] Afshar, N F. ; Deutsch, J ; Henninger, S ; Kožulović, D ; Bechlars, P ; AG, MTU Aero E.: Turbulence Anisotropy Analysis at the Middle Section of a Highly Loaded 3D Linear Turbine Cascade Using Large Eddy Simulation. In: *Global Power & Propulsion Technical Conference*

[3] Bear, Philip ; Wolff, Mitch ; Gross, Andreas ; Marks, Christopher R. ; Sondergaard, Rolf: Experimental investigation of total pressure loss development in a highly loaded low-pressure turbine cascade. In: *Journal of Turbomachinery* 140 (2018), Nr. 3

[4] Becker, Kai ; Heitkamp, Kathrin ; Kügeler, Edmund: Recent progress in a hybrid-grid CFD solver for turbomachinery flows. In: *Proceedings fifth European conference on computational fluid dynamics ECCOMAS CFD* Bd. 2010, 2010

[5] Bergmann, Michael ; Morsbach, Christian ; Ashcroft, Graham ; Kügeler, Edmund: Statistical error estimation methods for engineering-relevant quantities from scale-resolving simulations. In: *Journal of Turbomachinery* 144 (2022), Nr. 3

[6] Bode, Christoph ; Aufderheide, Thorben ; Kožulović, Dragan ; Friedrichs, Jens: The effects of turbulence length scale on turbulence and transition prediction in turbomachinery flows. In: *Turbo Expo: Power for Land, Sea, and Air* Bd. 45615 American Society of Mechanical Engineers, 2014, S. V02BT39A042

[7] Celik, Ishmail B. ; Ghia, Urmila ; Roache, Patrick J. ; Freitas, Christopher J.: Procedure for estimation and reporting of uncertainty due to discretization in CFD applications. In: *Journal of fluids Engineering-Transactions of the ASME* 130 (2008), Nr. 7

[8] Chanson, Hubert: *Applied hydrodynamics: an introduction to ideal and real fluid flows*. CRC press, 2009

[9] Daly, Bart J. ; Harlow, Francis H.: Transport equations in turbulence. In: *The physics of fluids* 13 (1970), Nr. 11, S. 2634–2649

[10] Deutsch, Johannes: *LES simulation.* personal communication, 2022

[11] Einstein, Albert: Die Grundlage der allgemeinen relativitätstheorie [AdP 49, 769 (1916)]. In: *Annalen der Physik* 14 (2005), Nr. S1 1, S. 517–571

[12] Emory, M ; Iaccarino, G: Visualizing turbulence anisotropy in the spatial domain

with componentality contours. In: *Center for Turbulence Research Annual Research Briefs* (2014), S. 123–138

[13] Farokhi, Saeed: *Aircraft propulsion*. John Wiley & Sons, 2014

[14] Favre, Alexandre J.: Formulation of the statistical equations of turbulent flows with variable density. In: *Studies in turbulence* (1992), S. 324–341

[15] Ferziger, Joel H. ; Perić, Milovan ; Street, Robert L.: *Computational methods for fluid dynamics*. Bd. 4. Springer, 2020

[16] Guide, TRACE U.: *Gamma-ReTheta transition model*. http://www.traceportal.de/userguide/trace/page_transitionGammaReTheta.html, 2021

[17] Guide, TRACE U.: *Viscous Blending Limiter*. https://www.trace-portal.de/userguide/trace/page_turbulenceModelExtensions.html, 2021

[18] Hilgenfeld, Lothar ; Pfitzner, Michael: Unsteady boundary layer development due to wake passing effects on a highly loaded linear compressor cascade. In: *J. Turbomach.* 126 (2004), Nr. 4, S. 493–500

[19] Hirsch, Charles: Numerical computation of internal and external flows. Vol. 2-Computational Methods for Inviscid and Viscous Flows. In: *Chichester* (1990)

[20] Kang, Shun ; Hirsch, Ch: Three dimensional flow in a linear compressor cascade at design conditions. In: *Turbo Expo: Power for Land, Sea, and Air* Bd. 78989 American Society of Mechanical Engineers, 1991, S. V001T01A047

[21] King, Roger: A review of vortex shedding research and its application. In: *Ocean Engineering* 4 (1977), Nr. 3, S. 141–171

[22] Kolmogorov, Andrei N.: The local structure of turbulence in incompressible viscous fluid for very large Reynolds numbers. In: *Proceedings of the Royal Society of London. Series A: Mathematical and Physical Sciences* 434 (1991), Nr. 1890, S. 9–13

[23] Krein, Axel ; Williams, Gareth: Flightpath 2050: Europe's vision for aeronautics. In: *Innovation for Sustainable Aviation in a Global Environment: Proceedings of the Sixth European Aeronautics Days, Madrid* 30 (2012)

[24] Langtry, Robin B. ; Menter, Florian R.: Correlation-based transition modeling for unstructured parallelized computational fluid dynamics codes. In: *AIAA journal* 47 (2009), Nr. 12, S. 2894–2906

[25] Lardeau, Sylvain ; Leschziner, MA: Unsteady Reynolds-averaged Navier-Stokes computations of transitional wake/blade interaction. In: *AIAA journal* 42 (2004), Nr. 8, S. 1559–1571

[26] Launder, Brian E. ; Sandham, Neil D.: *Closure strategies for turbulent and transitional flows*. Cambridge University Press, 2002

[27] Leggett, John: *Detailed investigation of loss prediction of an axial compressor cascade at off-design conditions in the presence of incident free-stream disturbances using large eddy simulations*, University of Southampton, Diss., 2018

[28] Leipold, Robert ; Boese, Matthias ; Fottner, Leonhard: The influence of technical surface roughness caused by precision forging on the flow around a highly loaded compressor cascade. In: *J. Turbomach.* 122 (2000), Nr. 3, S. 416–424

[29] LeVeque, Randall J.: *Finite volume methods for hyperbolic problems*. Bd. 31. Cambridge university press, 2002

[30] Lieblein, Seymour: Loss and stall analysis of compressor cascades. In: *Journal of basic engineering* 81 (1959), Nr. 3, S. 387–397

[31] Lowson, MV: Theoretical analysis of compressor noise. In: *The Journal of the Acoustical Society of America* 47 (1970), Nr. 1B, S. 371–385

[32] Matha, Marcel ; Morsbach, Christian ; Bergmann, Michael: A comparison of methods for introducing synthetic turbulence. In: *ECCOMAS–ECFD 2018-6th European Conference on Computational Mechanics (Solids, Structures and Coupled Problems)/7th European Conference on Computational Fluid Dynamics*, 2018

[33] Medic, Gorazd ; Zhang, Vicky ; Wang, Guolei ; Joo, Jongwook ; Sharma, Om P.: Prediction of transition and losses in compressor cascades using large-eddy simulation. In: *Journal of Turbomachinery* 138 (2016), Nr. 12, S. 121001

[34] Morsbach, Christian ; Franke, Martin: Analysis of a synthetic turbulence generation method for periodic configurations. In: *Direct and Large-Eddy Simulation XI* Springer, 2019, S. 169–174

[35] Munson, Bruce R. ; Young, Donald F. ; Okiishi, Theodore H.: Fundamentals of fluid mechanics. In: *Oceanographic Literature Review* 10 (1995), Nr. 42, S. 831

[36] Nicoud, Franck ; Ducros, Frédéric: Subgrid-scale stress modelling based on the square of the velocity gradient tensor. In: *Flow, turbulence and Combustion* 62 (1999), Nr. 3, S. 183–200

[37] Nürnberger, Dirk: Implizite zeitintegration für die simulation von turbomaschinenströmungen. (2004)

[38] Parneix, S ; Laurence, D ; Durbin, PA: A procedure for using DNS databases. (1998)

[39] Piomelli, U: Large eddy simulations in 2030 and beyond. In: *Philosophical Transactions of the Royal Society A: Mathematical, Physical and Engineering Sciences* 372 (2014), Nr. 2022, S. 20130320

[40] Pope, Stephen B. ; Pope, Stephen B.: *Turbulent flows*. Cambridge university press, 2000

[41] Raj, R ; Lakshminarayana, B: Characteristics of the wake behind a cascade of airfoils. In: *Journal of Fluid Mechanics* 61 (1973), Nr. 4, S. 707–730

[42] Reynolds, B ; Lakshminarayana, B ; Ravindranath, A: Characteristics of the near wake of a compressor of a fan rotor blade. In: *AIAA Journal* 17 (1979), Nr. 9, S. 959–967

[43] Reynolds, Osborne: IV. On the dynamical theory of incompressible viscous fluids and the determination of the criterion. In: *Philosophical transactions of the royal society of london.(a.)* (1895), Nr. 186, S. 123–164

[44] Richardson, Lewis F.: IX. The approximate arithmetical solution by finite differences of physical problems involving differential equations, with an application to the stresses in a masonry dam. In: *Philosophical Transactions of the Royal Society of London. Series A, Containing Papers of a Mathematical or Physical Character* 210 (1911), Nr. 459-470, S. 307–357

[45] Richardson, Lewis F. u. a.: Weather Prediction by Numerical Process. (2007)

[46] Richardson, Lewis F. ; Gaunt, J A.: VIII. The deferred approach to the limit. In: *Philosophical Transactions of the Royal Society of London. Series A, containing papers of a mathematical or physical character* 226 (1927), Nr. 636-646, S. 299–361

[47] Schlichting, Hermann ; Gersten, Klaus: *Boundary-layer theory.* springer, 2016

[48] Shi, Lei ; Ma, Hongwei ; Yu, Xinghang: POD analysis of the unsteady behavior of blade wake under the influence of laminar separation vortex shedding in a compressor cascade. In: *Aerospace Science and Technology* 105 (2020), S. 106056

[49] Shur, Michael L. ; Spalart, Philippe R. ; Strelets, Michael K. ; Travin, Andrey K.: Synthetic turbulence generators for RANS-LES interfaces in zonal simulations of aerodynamic and aeroacoustic problems. In: *Flow, turbulence and combustion* 93 (2014), S. 63–92

[50] Singh, Pushpendra ; Joshi, Shiv D. ; Patney, Rakesh K. ; Saha, Kaushik: The Fourier decomposition method for nonlinear and non-stationary time series analysis. In: *Proceedings of the Royal Society A: Mathematical, Physical and Engineering Sciences* 473 (2017), Nr. 2199, S. 20160871

[51] Spalart, Philippe R.: Philosophies and fallacies in turbulence modeling. In: *Progress in Aerospace Sciences* 74 (2015), S. 1–15

[52] Sturm, Hannes ; Dumstorff, Gerrit ; Busche, Peter ; Westermann, Dieter ; Lang, Walter: Boundary layer separation and reattachment detection on airfoils by thermal flow sensors. In: *Sensors* 12 (2012), Nr. 11, S. 14292–14306

[53] Tyacke, James C. ; Tucker, Paul G.: Future use of large eddy simulation in aero-engines. In: *Journal of Turbomachinery* 137 (2015), Nr. 8, S. 081005

[54] Versteeg, Henk K. ; Malalasekera, Weeratunge: *An introduction to computational fluid dynamics: the finite volume method*. Pearson education, 2007

[55] Wilcox, David C. u. a.: *Turbulence modeling for CFD*. Bd. 3. DCW industries La Canada, CA, 2006

[56] Xiong, Zhongmin ; Lele, Sanjiva K.: Stagnation-point flow under free-stream turbulence. In: *Journal of fluid mechanics* 590 (2007), S. 1–33

[57] You, Donghyun ; Mittal, Rajat ; Wang, Meng ; Moin, Parviz: Computational methodology for large-eddy simulation of tip-clearance flows. In: *AIAA journal* 42 (2004), Nr. 2, S. 271–279

[58] You, Donghyun ; Wang, Meng ; Moin, Parviz ; Mittal, Rajat: Large-eddy simulation analysis of mechanisms for viscous losses in a turbomachinery tip-clearance flow. In: *Journal of Fluid Mechanics* 586 (2007), S. 177–204

[59] Zou, Tengda ; Lee, Cunbiao: The effect of the wake on the separated boundary layer in a two-stage compressor. In: *Physics of Fluids* 33 (2021), Nr. 3, S. 034125